Geophysical Journal International

Geophys. J. Int. (2019) **219,** 1698–1716
Advance Access publication 2019 August 29
Marine geosciences and applied geophysics

doi: 10.1093/gji/ggz390

Mineral exploration with 3-D controlled-source electromagnetic method: a synthetic study of Sukhoi Log gold deposit

M. Malovichko[1,2] A.V. Tarasov,[3] N. Yavich[1,2] and M.S. Zhdanov[2,4,5]

[1] *Skolkovo Institute of Science and Technology, Center for Computational and Data-Intensive Science and Engineering, Moscow, Russia.*
E-mail: m.malovichko@skoltech.ru
[2] *Moscow Institute of Physics and Technology, Applied Computational Geophysics Lab, Dolgoprudny, Russia*
[3] *Saint-Petersburg University, Institute of Earth sciences, St.-Petersburg, Russia*
[4] *University of Utah, Department of Geology & Geophysics, Salt Lake City, Utah, USA*
[5] *TechnoImaging, Salt Lake City, Utah, USA*

Accepted 2019 August 28. Received 2018 December 6; in original form 2019 August 9

SUMMARY

This paper presents a feasibility study of using the controlled-source frequency-domain electromagnetic (CSEM) method in mineral exploration. The method has been widely applied for offshore hydrocarbon exploration; however, nowadays this method is rarely used on land. In order to conduct this study, we have developed a fully parallelized forward modelling finite-difference (FD) code based on the iterative solver with contraction-operator preconditioner. The regularized inversion algorithm uses the Gauss–Newton method to minimize the Tikhonov parametric functional with the Laplacian-type stabilizer. A 3-D parallel inversion code, based on the iterative finite-difference solver with the contraction-operator preconditioner, has been evaluated for the solution of the large-scale inverse problems. Using the computer simulation for a synthetic model of Sukhoi Log gold deposit, we have compared the CSEM method with the conventional direct current sounding and the CSEM survey with a single remote transmitter. Our results suggest that, a properly designed electromagnetic survey together with modern 3-D inversion could provide detailed information about the geoelectrical structure of the mineral deposit.

Key words: Controlled source electromagnetics (CSEM); Inverse theory; Electromagnetic theory; Electrical properties; Numerical solutions.

1 INTRODUCTION

The 3-D electromagnetic (EM) inversion methods and acquisition equipment have been advanced considerably over the recent decades. For general reviews of EM geophysics in the context of mineral exploration, we refer to Oldenburg & Pratt (2007), Vallée *et al*. (2011) and Farquharson & Lelièvre (2017). Still, the geophysical EM surveys often are not consistent with the required accuracy to reconstruct the real geological media. With respect to 3-D surveying, the choice is usually made between the airborne EM methods, active-source time-domain measurements, direct current (dc) methods and, sometimes, the natural/CSEM methods with planar excitation.

The airborne EM methods, both natural- and active-source, with their rapid spatial acquisition are able to cover large areas in a short time (Zhdanov 2010; Vallée *et al*. 2011; Yin *et al*. 2015). Recent advances in 3-D inversion of large-scale EM data made it possible to rigorously invert in 3-D entire airborne geophysical surveys over large areas (Cox & Zhdanov 2007; Cox *et al*. 2012; Čuma *et al*. 2016; Zhdanov *et al*. 2018). However, even with 3-D interpretation of the airborne data, the follow-up ground surveys are often required to obtain a more detailed information about the subsurface geology of an area of the potential mineral deposit.

The ground-based natural-field methods including MT/AMT are successfully applied to the ore prospecting in certain cases. For a comprehensive review of the MT/AMT methods we refer to (Chave & Jones 2012; Jansen & Cristall 2017; Zhdanov 2018). The 3-D inversion is routinely performed on MT data sets. The downside of these methods is that they inherit relatively low resolution due to the plane-wave excitation. The same is true for the CSMT/CSAMT/CSRMT and VLF methods, although they use a controlled source in the far-field zone. Such a source generates a non-uniform plane wave (that is, the equiphase surfaces are horizontal planes, but the amplitude of the field changes along them), which has low sensitivity to thin horizontally oriented inhomogeneities.

The ground-based time-domain methods have a long history of application in mineral geophysics. We refer to Strack (1999) for a review of early developments, as well as the LOTEM technique, which had been widely applied in Europe. In principle, a 3-D image of the subsurface can be obtained using closely located transmitter

and receiver without the necessity to have large range of separations. The spatial resolution of these methods is high, especially if a grounded source is used. However, the time-domain forward modelling, and, consequently, the corresponding inverse problem, is a very complex mathematical task, which also demands large computing resources. Several successful 3-D examples have been published (Newman & Commer 2005; Oldenburg *et al*. 2013). However, those examples are quite restrictive in the sense they use very sparse irregular acquisition grids. To our opinion, the enormous potential of these methods is still not properly explored.

The dc methods have undergone a rapid expansion to the 3-D implementation over the last decade (Günther *et al*. 2006; Stummer *et al*. 2006; Loke *et al*. 2013; Shore 2017; Uhlemann *et al*. 2018). Commercially available dc systems can operate dense receiver/transmitters grids with fully 3-D acquisition geometry. The high-resistive layers, however, limit the depth of penetration of the dc; otherwise these methods may be used for deep investigations. It is generally accepted that their resolution is lower than that of the alternating-current EM methods, especially in high-conductive environments, where the inductive attenuation provides additional information.

The frequency-domain CSEM sounding, in which depth of investigation depends both of the frequency and the transmitter–receiver separation, was actively used in the 1950s–1960s. The theoretical background and history of its application is presented in many textbooks, for example in (Vanyan *et al*. 1967; Kaufman & Keller 1983; Zhdanov & Keller 1994; Zhdanov 2009, 2018). This method is known to provide high spatial resolution, especially if the EM field is emitted by a grounded cable. From the numerical standpoint, the method admits independent computational grids for each monochromatic source making large inverse problems be computationally tractable. The method has been adopted for marine EM surveys (Constable 2010; Key 2016; Morten *et al*. 2016). However, nowadays such measurements almost never conducted in the land applications, mostly because it is difficult to deploy many source–receiver pairs on the ground. We will refer such land-based multifrequency multi-offset measurements as the (land) CSEM.

Critical elements of such a method, namely, the transmitter/receiver operation and 3-D inversion capabilities, have recently undergone substantial development. Modern dc systems can handle dense receiver–transmitter grids with thousands transmitter–receiver pairs. Moreover, those measurements, despite being interpreted as the dc data, are conducted at some frequency albeit low. Measurements with alternating current that is fed into orthogonal grounded cables are routinely collected by the CSAMT community (Li & Pedersen 1991; Kalscheuer *et al*. 2015). The recently developed transmitters with three current-carrying source wires specifically target the land CSEM applications (Grayver *et al*. 2014).

A numerical feasibility study of the land CSEM method was presented in (Wirianto *et al*. 2010). Recently, several trial surveys have been reported (Streich *et al*. 2011; Grayver *et al*. 2014; Tietze *et al*. 2015; Bretaudeau *et al*. 2017; Schaller *et al*. 2018). In all cases, the subsurface was composed by a sedimentary sequence with gentle folds and low conductivity contrast. Very sparse irregular acquisition grids (1–5 transmitter stations) were deployed in all the cases. Thus, applicability of the land CSEM technique to mining exploration with its 3-D high-contrast models has not been studied yet.

The 3-D forward modelling and inversion methods have been advanced recently to the point, when a large-scale 3-D CSEM inversion becomes possible. An efficient numerical method for EM modelling, based on the iterative solution of the FD matrix with a contraction-operator preconditioner, has been proposed by Yavich & Zhdanov (2016). The distinguished properties of the algorithm are that it has linear memory consumption and its runtime has mild dependency on lateral conductivity contrast. Both properties are advantageous for mineral geophysics, where high conductivity contrast results in huge numerical grids.

Our motivation for this research is twofold. First, we investigate capabilities of multifrequency multi-offset CSEM method in mineral applications and compare sensitivity of such measurements with conventional dc data. Secondly, we study the 3-D EM inversion based on the iterative finite-difference (FD) solver with the contraction-operator preconditioner and evaluate its applicability to large 3-D inverse problems.

We use a detailed model of sediment-hosted Sukhoi Log gold deposit located in Eastern Siberia, where the strong conductivity contrast forms an excellent target for EM geophysical methods. Nevertheless, the deposit has been discovered and, subsequently, studied mainly by geochemical and geological means, including a very extensive drilling program. The deposit was explored by various geophysical methods in 1970s; however, only a basic qualitative interpretation was available at that time. The possibilities of modern 3-D EM inversion have been never used.

In this paper, we review the geological and geophysical data obtained over Sukhoi Log. A volumetric electrical conductivity model of the deposit has been created based on drilling data and other previous geological and geophysical studies. We have calculated the EM responses from 3-D conductivity model and carried out a 3-D synthetic inversion study with three types of acquisition geometry. Our results suggest that, a properly designed EM survey together with modern 3-D inversion may bring detailed information about the structure of the subsurface, thus significantly reducing the exploration cost for large black-shale-hosted gold deposits. Our conclusions may be generalized for other geological settings with a similar geological pattern, that is, a concealed orebody with strong structural control in a high-contrast mostly resistive environment.

2 FORWARD PROBLEM

We consider the following time-harmonic system of partial differential equations with respect to the electric field $\mathbf{E}(x, y, z)$:

$$curl\ curl\ \mathbf{E} - i\omega\mu_0\sigma\ \mathbf{E} = i\omega\mu_0\mathbf{J}, \tag{1}$$

where ω is the source angular frequency, μ_0 is the magnetic permeability of the free space, $\sigma(x, y, z)$ is the electric conductivity, $\mathbf{J}(x, y, z)$ is the source current density. Eq. (1) are completed with zero Dirichlet boundary conditions in some bounded domain V and are solved numerically.

Realistic modelling of 3-D geological structures results in discrete problems with the number of unknowns on the order of 10^7 and even more. Within the inversion process, thousands of such problems should be solved. Thus, efficient and economic numerical solution of the forward problem is of paramount importance. We have discretized Eq. (1) with the finite-difference (FD) method on a staggered non-uniform grid with electric fields attached to the edges. To avoid excessive gridding near the source, we preferred the anomalous EM field formulation of the forward modelling problem.

The FD system of linear equations typically has a very high condition number; we thus solved it with the preconditioned BiCGStab method. The pre-conditioner combines a discrete separation of variables as well as a special transformation resulting in a contraction

operator (Yavich & Zhdanov 2016). The spectral properties of the preconditioned matrix are invariant of frequency, grid size and geometry and they have only moderate dependence on the lateral conductivity contrast, meaning the run time increases slowly as the conductivity contrast grows. The algorithm was further leveraged with OpenMP shared memory parallelization as described in (Yavich *et al*. 2017). This preconditioner was shown to be robust and memory-economical.

3 INVERSE PROBLEM

Let W be a 3-D domain, discretized into M rectangular cells. We wish to find the values of σ sampled in the cell's centres, based on the measured components of the electric field, $\boldsymbol{E}$. Let the total number of input data points be equal to N. We formulate the inversion as the unconstrained minimization of the following parametric functional (Zhdanov 2002, 2015):

$$P(\boldsymbol{m}) = \|\mathbf{W}(\mathcal{A}(\mathbf{m}) - \mathbf{d})\|^2 + \alpha \left\|\mathbf{L}^{1/2}(\mathbf{m} - \mathbf{m}_0)\right\|^2 \underset{\mathbf{m},\alpha}{\rightarrow} min, \quad (2)$$

where $\mathbf{m} \in R^M$ is the model vector (values of $\log_{10}\sigma$ sampled at cell centres), $\mathbf{m}_0$ is the initial model, $\mathbf{d} \in C^N$ is vector of input data (that is, values of electric field $\mathbf{E}$, both the real and imaginary parts), $\mathbf{W}$ is a diagonal matrix of data weights, α is the regularization parameter, $\mathbf{L}$ is a matrix of discrete negative Laplacian operator. A non-linear forward-modelling operator $\mathcal{A}$ maps a given model to the data.

The 3-D EM optimization problem (2) is usually solved by methods of the two classes: the gradient-based methods, possibly with preconditioning, such as non-linear conjugate-gradient (NLCG) and L-BFGS solvers, and Newton's methods and its variants. Both classes of methods have been extensively covered in literature. The NLCG/L-BFGS methods are less demanding in terms of computational load and memory consumption but may suffer from slow convergence at complicated models. There are two approaches, which aim to mitigate this shortcoming: a diagonal preconditioner of Newman & Boggs (2004) and the integral-sensitivity approach of Zhdanov (2002). These approaches are essential to achieve a tolerable convergence rate and, in fact, are very similar. Recent examples with these methods include (Commer & Newman 2008) and (Čuma *et al*. 2017). The Newton's method (usually in form of the Gauss–Newton method) ensures fast convergence but has high computational and/or memory complexity due to the need to solve the system of linear equations with the Hessian matrix. This difficulty can be overcome only partially by using the modern massively parallel distributed memory clusters (for example, Grayver *et al*. 2013; Wang *et al*. 2018).

We have tested several approaches to EM inversion (Malovichko *et al*. 2018). The optimization techniques based on the diagonal approximation of the Hessian matrix behaved poorly on the Sukhoi Log model. We attribute this to the fact that the Hessian matrix of low-frequency EM operator $\mathcal{A}$ is not diagonally dominant in the frequency range we tested (0.001–500 Hz). In combination with a high-contrast 3-D model it led to slow convergence or even to the breakdown of the non-linear optimization procedure. Therefore, we used the Gauss–Newton method to minimize problem (2).

The model is iterated as $\mathbf{m}_n = \mathbf{m}_{n-1} + \gamma_n \mathbf{p}_n$, where $\mathbf{p}_n$ is the search direction, $\gamma_n \in [0, 1]$ is the step size. In the framework of Newton method, $\mathbf{p}_{n+1}$ is a solution to the following system of linear equations:

$$(\mathbf{J}^*\mathbf{W}^*\mathbf{W}\mathbf{J} + \alpha\mathbf{L})\,\mathbf{p}_{n+1} = \mathbf{J}^*\,\mathbf{W}^*\mathbf{W}\mathbf{r}_n - \alpha\mathbf{L}(\mathbf{m}_n - \mathbf{m}_0), \quad (3)$$

where $\mathbf{r}_n = \mathbf{d} - \mathcal{A}(\mathbf{m}_n)$ is the data residual, $\mathbf{J}$ is the Jacobian of the operator $\mathcal{A}$ at $\mathbf{m}_n$:

$$\mathbf{J} = \left.\frac{\partial \mathcal{A}}{\partial \mathbf{m}}\right|_{\mathbf{m}=\mathbf{m}_n}. \quad (4)$$

Matrix $\mathbf{J}^*\mathbf{W}^*\mathbf{W}\mathbf{J}$, which approximates the Hessian of the first term in (2), is dense, Hermitian and ill-conditioned. It is not diagonally dominant at low source frequencies. In order to solve system (3) iteratively, and to compute term $\mathbf{J}^*\mathbf{W}^*\mathbf{W}\mathbf{r}_n$, we need to multiply the Jacobian and conjugated Jacobian by corresponding vectors. Thus, we consider the products of the form:

$$\mathbf{w} = \mathbf{J}^*\,\mathbf{v}, \mathbf{w} \in R^M, \mathbf{v} \in C^N, \quad (5)$$

and

$$\mathbf{y} = \mathbf{J}\mathbf{x}, \mathbf{x} \in R^M, \mathbf{y} \in C^N. \quad (6)$$

Since the computations are run in parallel on several MPI ranks, the resulting vector is assembled from the results of each rank. Specifically, assuming that there are K MPI ranks, we can write:

$$\mathbf{w} = \sum_{k=1}^{K} \mathbf{J}_k^* \mathbf{v}_k\,, \quad (7)$$

and

$$\mathbf{y}_k = \mathbf{J}_k\,\mathbf{x}_k, \quad \mathbf{y} = \left[\mathbf{y}_1^T..\mathbf{y}_K^T\right]^T. \quad (8)$$

Here, the lower indices indicate parts of matrices and vectors that correspond to kth MPI rank. Note that (5) as well as the result of summation in (7) is real-valued up to round-off errors.

In the programming implementation, expressions (7) and (8) become significantly more complicated due to the necessity to take into account the difference between the inversion grid and finite-difference grids of each source, the non-linear relationship between electrical conductivity and inversion parameters, and the fact that entries of the data vector are given by an interpolation operator applied to the discrete FD solution. These points have been addressed in literature in general, for example, (Egbert & Kelbert 2012). We cover particularities of our implementation in Appendix A.

We solve the linear subproblem (3) by the conjugate gradient (CG) method, so that the system matrix never formed explicitly. A non-linear 1-D search procedure was used to find a suitable value of γ_n. The regularization parameter is selected on each iteration as $\alpha_n = \alpha_0/2^n$, $n = 0, 1, ..$, where α_0 is some initial value. The progress of inversion is controlled by the value of the normalized misfit

$$e_n = \|\mathbf{W}\mathbf{r}_n\|/N, \quad (9)$$

which is commonly referred to as ERMS. Newton's iterations are terminated when $e_n \leq 1$ for some n.

The problem (2) is solved with MPI/OpenMP parallelization. The different source locations and frequencies are distributed across a number of compute nodes. In each node several computer cores work together on the forward problem and the Fréchet derivative computations.

4 SYNTHETIC STUDY OF SUKHOI LOG GOLD DEPOSIT

4.1 Geological setting

Sukhoi Log is a world-class sediment-hosted gold deposit. The deposit has been discovered in 1961 and was extensively explored

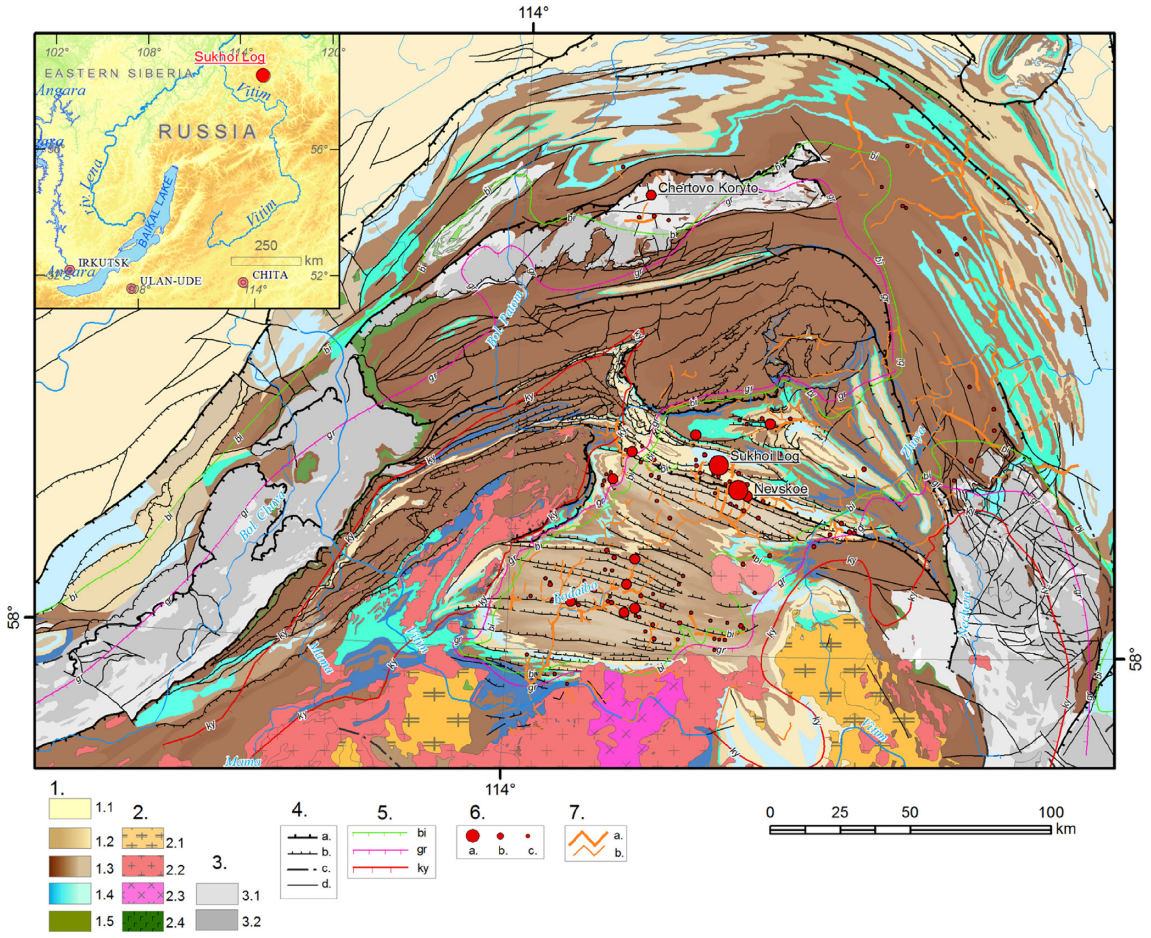

Figure 1. Regional geological position of Sukhoi Log: the Baikal-Patom fold belt and Lena Gold Province. Legend: 1. Sedimetary formations: 1.1 – Siberian platform series (from Vendian to Cambrian age, terrigeneous and carbonate formations), 1.2 – strongly deformed Riphean-Vendian carbonate-terrigeneous rocks (calcarenites, sandstones, limestones, clay marls, shales with limestone interbeds, black shales), 1.3 – lower and middle Riphean predominantly terrigeneous formations (conglomerates, greywacks, arkose, aleurolites and shales/black shales), 1.4 – carbonate formations (limestones, marls, marbles), 1.5 – terrigeneous-volcanogenic sequences in lower part of Riphean formations (conglomerates with metavolcanic rocks and interbeds of banded iron formation). 2. Palaeozoic intrusive rocks: 2.1 – sienite, 2.2 – granite 2.3 – diorite (parts of Angara-Vitim batholith), 2.4 – gabbro; 3. Large-scale basement uplift (Archean and Lower Proterozoic): 3.1 – shists, migmatites, gneisses, 3.2 – undifferentiated ancient intrusive rocks; 4. Tectonics: a. – main thrust zones, b. – thrusts, c. – main faults and fracture zones, d. – faults; 5. Boundaries of regional metamorphic facies: bi – upper greenshist (biotitic zone), gr – garnet or amphibolite zone, ky – kyanite zone; 6. Gold deposits: a. – large, b – middle, c. – small; 7. Gold placers: a. – rich, b. – ordinary.

in 1970s by Geological Survey of the USSR. The deposit located in Eastern Siberia, 900 km northeast of Irkutsk (Fig. 1). According to the recent data, gold reserves of Sukhoi Log are estimated as 62.8 Moz of gold, that is 930 Mt of gold ore with the average grade of 2.1 g/t. This is the largest Russian gold deposit, which has been studied by many researchers (Buryak & Khmelevskaya 1997; Distler *et al*. 2004; Wood & Popov 2006; Yudovskaya *et al*. 2016).

The deposit is located within the Lena Gold Province (LGP) as presented in Fig. 1. The LGP covers the northern part the Baikal-Patom Highland, which forms an arc-shaped region located between Lake Baikal on the southwest and Chara River on the east. The Baikal-Patom Highland is a fold belt in the southern margin of Siberian Platform. Its boundaries correspond to the outcrops of intensively deformed terrigenous carbonate-carbonaceous Mesoproterozoic and Neoproterozoic (Riphean-Vendian) metasedimentary formations (Rundqist *et al*. 1992). Its eastern, northern and western flanks are bordered with undeformed sedimentary cover of the Siberian Platform. The southern border corresponds to the northern edge of a giant Paleozoic granitoid massif known as Angara-Vitim batholith. A number of granitiod domes trace a fault system known as Muya deep fault, which extends from the northern coast of Lake Baikal on the west to the northern flank of the Archean-Proterozoic Muya terrain on the east.

Gold mineralization and placer deposits mostly occur within the Mama-Bodaibo Synclinorium in the central part of Baikal-Patom fold belt. Strongly folded Upper Riphean (1000 Ma) and Vendian (600 Ma) metasedimentary rocks fill the Mama-Bodaibo Synclinorium with the total thickness of more than 10 km. Metasediments are metamorphosed to greenschist facies and sometimes to higher-grade facies, and are intruded by granites of Carboniferous age. A small outcrop of these granites, which is known as the Konstantinovsky stock, is located 3 km southwest from Sukhoi Log. Gravity data suggest that it is a part of the hidden large-scale Ugahan granitoid massif (Distler *et al*. 2004).

Apart from Sikhoi Log, several smaller deposits have been discovered within the LGP, including Verninskoye (7 km southeast from Sukhoi Log), Nevskoe, Golets Vysochaishy, and Chertovo Koryto. Most deposits and gold occurrences can be categorized into three mineralization types: the gold-sulfide type (pyrrhotite–pyrite–arsenopyrite); the gold–sulfide–quartz veins (quartz-carbonate with

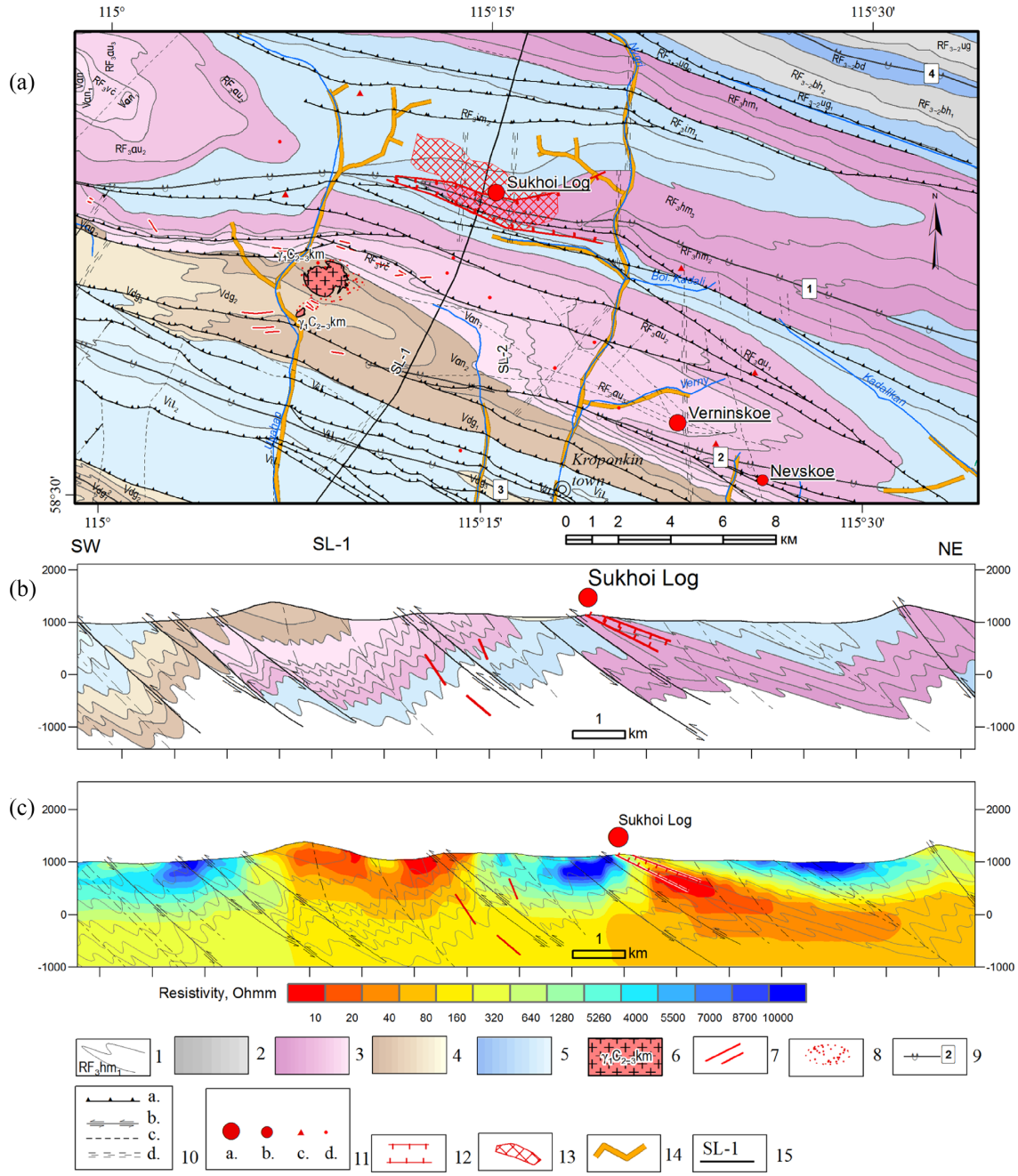

Figure 2. Location and surface geology of the Sukhoi Log deposit. Panel (a): Local surface geology. Panel (b): Schematic cross section along line SL-1. Panel (c): resistivity model along line SL-1 obtained by inversion of 2D AMT data (Sushinskiy 2015). Legend: 1. Geological boundaries and formation indexes. 2–5. Lithological formations (the colour indicates age; colour intensity corresponds to the relative age inside the same stratigraphic unit): 2–Lower Riphean terrigeneous formations (carbonaceous shales, siltstones, sandstones); 3–Upper Riphean and Vendian terrigeneous-carbonate formation (carbonaceous shales, siltstones, sandstones and limestones); 4–manly terrigeneous formations (arkosic sandstones, siltstones, subordinate amount of shales); 5–manly carbonate formations (limestones and carbonate shales, siltstones, sandstones). 6–Paleozoic (C2–3) granite (Konstantinovky stock). 7. Paleozoic dikes (porphyric granite and aplite). 8. Hornfels shell around a granite massif. 9. Axes of main anticlines (1– the Sukhoi Log anticline). 10. Tectonic elements: a—main thrusts (on the map), b—thrusts (in cross-sections), c—inferred faults, d—fracture zones; 10–Gold deposit and occurrences: a—large deposits, b—middle deposits, c—small deposits, d—gold occurrences. 12. Mineralized zone of Sukhoi Log. 13. The main ore body (grade > 0.5 g/t). 14. Gold alluvial placers. 15. The section line that corresponds to cross-sections (B) and (C).

pyrite and other sulfides), and gold-bearing quartz veins. According to Goldfarb *et al*. (2005) they can be classified as the orogenic-type deposits in metamorphic terranes. They are usually located adjacent to the first-order deep-crustal fault zones and have complex geological history with no apparent relation to granitoid magmatism.

The geological structure of Sukhoi Log and morphology of the ore mineralization are well studied, mostly during a very extensive exploration program undertaken in the 1970s, which included 847 boreholes, 11 km of underground drives, 100 km of trenches, and many tens of thousands of samples and gold assays (Wood & Popov

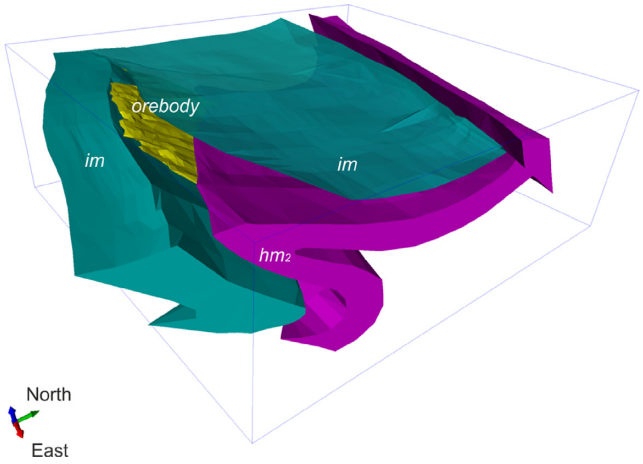

Figure 3. Four out of five geological bodies used for the 'true' model creation. Index *im* corresponds to the upper and lower limbs of the Imnyah formation. Index hm_2 corresponds to the Middle Khomolho formation. The Lower Khomolho (hm_1), which is not shown here, is located between *im* and hm_2. The Upper Khomolho (hm_3) is included in the background. The surfaces of the five bodies in DFX format are attached to the on-line version of this article.

Table 1. Resistivity of the main geological formations.

#	Formation	Resistivity, Ωm
1	Quaternary sediments	250
2	Imnyah (*im*), normal limb	3000
3	Imnyah (*im*), overturned limb	3000
4	Main orebody	5
5	Lower Khomolho (hm_1)	100
6	Middle Khomolho (hm_2)	50
7	Upper Khomolho (hm_3)	300
8	Air	1E8

2006). The deposit occurs in the core of the very tight, south-verging Sukhoi Log anticline of the third order, which is located in the hanging wall of a south-verging thrust fault (Fig. 2).

The anticline plunges gently to the west-northwest and its axial surface dips 20° to 30° north-northeast (Fig. 2a). The mineralized zone forms a gently dipping tabular body parallel to the axial plane of the fold (Fig. 2b). The zone extends approximately 2000 m along strike and 700 m downdip with the average thickness of 70–100 m. The main ore zone of the Sukhoi Log deposit consists of disseminated pyrite and bedding-parallel pyrite-quartz veinlets, hosted in Neoproterozoic (upper Riphean, RF_3) black carbonaceous shales and siltstones of Khomolho formation (*hm*). Distribution of gold in the deposit strongly depends on the morphology of quartz-sulfide mineralization. The quartz-sulfide veinlets and their structural parageneses have been studied in detail (Buryak & Khmelevskaya 1997; Large *et al*. 2007). The higher-grade gold mineralization is presented in folded pyrite-quartz veinlets. These veinlets are 2 to 3 cm thick, on average, and contain 30 to 50 vol per cent pyrite and other sulfides in lower concentration (arsenopyrite, chalcopyrite, pyrrhotite, galena, sphalerite). The averaged total percentage of sulfides of all pyrite types in the mineralized zone is less than 3.5 per cent and varies from 0.5 per cent to 5 per cent. Au grade varies from 0.1 to 360 ppm with the mean of 65 ppm for the folded pyrite-quartz veinlets.

The host rocks in the axial part of the Sukhoi Log anticline are intensively hydrothermally altered. The dominant minerals in alteration zone are quartz (30–50 vol per cent), sericite (35–50 vol per cent), and carbonate (5–30 vol per cent). There are evidences of correlation between the gold mineralization and the carbonate alteration with abundance of Fe-Mg and siderite porhyroblasts. The host rocks in the ore zone are also enriched with organic carbon (0.2–3.5 wt per cent) and Na_2O (0.6–2.2 wt per cent).

From 1970s up to 2013, the deposit has been studied by many geophysical methods, including detailed gravity and magnetic surveys (both airborne and ground-based) and a number of dc and IP electrical methods (including electrical profiling, vertical electrical soundings, downhole measurements, and the spontaneous polarization method). A small 2D AMT survey was carried out in 2013 for testing purposes (Fig. 2c). In contrast to geological data, geophysical accounts mostly exist in form of internal technical reports in a number of archives. One of the most systematic descriptions of geophysical data from Sukhoi Log is given in (Tarasov & Gurin 2016).

It was established that, the EM methods, including controlled-source EM, dc and IP measurements, significantly outperform other geophysical methods in detecting the main mineralization zone. The carbonaceous black shales of the Khomolho formation have low resistivity (< 100 Ohm m) and carbonate rocks of Imnyah formation (*im*) on the wings of the anticline have relatively high resistivity (> 1000 Ohm m). The gold-bearing quartz-sulfide mineralization is located in a zone of extremely low resistivity (<1–10 Ohmm) in the axial plane of the anticline. This low resistivity zone appeared due to graphite films in the cleavage planes as a result of tectonic extrusion of metamorphosed organic matter from carbonaceous shales. This arrangement creates a strong resistivity contrast between the upper unit of Khomolho formation (hm_3), which controls the localization of the main orebody, and the high-resistive Imnyah rocks.

We created a conductivity model of Sukhoi Log, based on surfaces of five main geological formations, which were digitized from field reports (Fig. 3). These bodies in AutoCAD DFX format (http://images.autodesk.com/adsk/files/autocad_2012_pdf_dxf-reference_enu.pdf) are attached to the electronic version of the article. We added a 100 m layer on the top of the model, which mimics Quaternary sediments. The conductivity of each body was set to a constant value, as summarized in Table 1.

In this study we use a local coordinate system with X-, Y-, and Z-axis pointing eastward, southward, and downward, respectively. We neglected the topography assuming that the air-ground interface is flat. The top face of our model at $z = 0$ correspond to elevation level 1100 m. The model was discretized with 25 m cubical cells. The model referred below as *the true model*, is presented in Fig. 4. The model in VTK file format (https://vtk.org/wp-content/uploads/2015/04/file-formats.pdf) and as a simple array of floats is attached to the article.

The large size and relatively simple geological structure of Sukhoi Log makes it an ideal target for testing various geological, geochemical, and geophysical methods.

4.2 Numerical experiment 1

In the first numerical experiment we simulated the multi-frequency multi-offset CSEM method. All sources and receivers were Y-electric dipoles, located at $z = 0$. The acquisition grid consists of 24 source stations, located on a grid 1.5 km × 1.5 km and 187 receiver stations placed on a grid 500 m × 500 m (Fig. 5a).

In each source station there were four monochromatic sources at frequencies 1, 10, 100 and 500 Hz. This frequency range was bounded from below by the dc limit, whereas its upper bound was

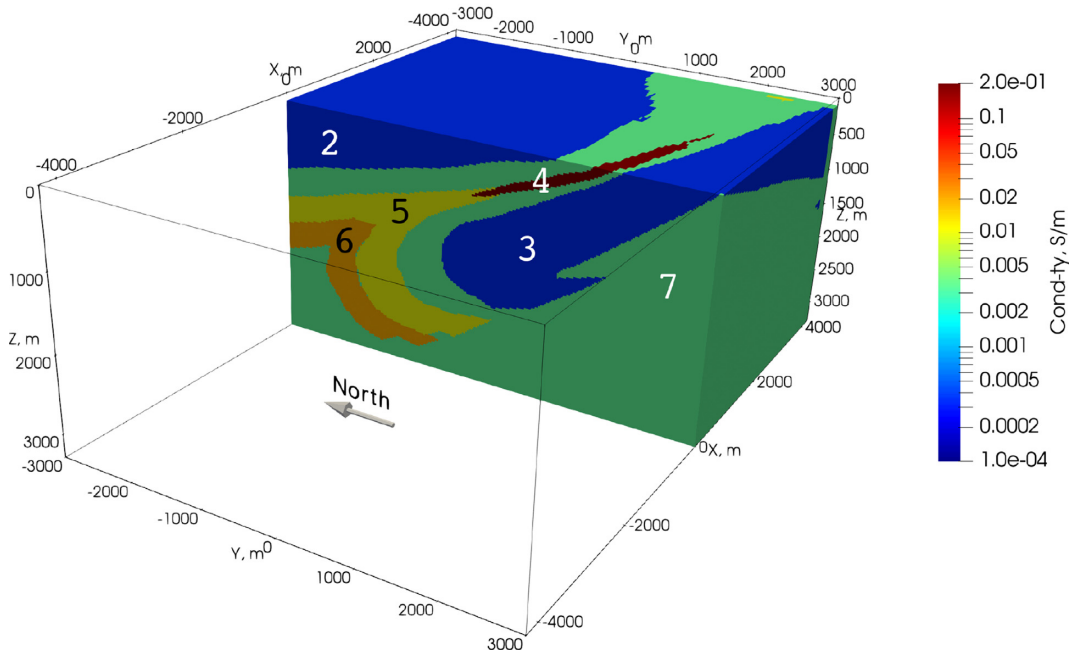

Figure 4. The cross-section of Sukhoi Log model used in numerical experiments. The numbers correspond to those in Table 1. The 1st and 8th layers (the cover and the air, respectively) are not shown.

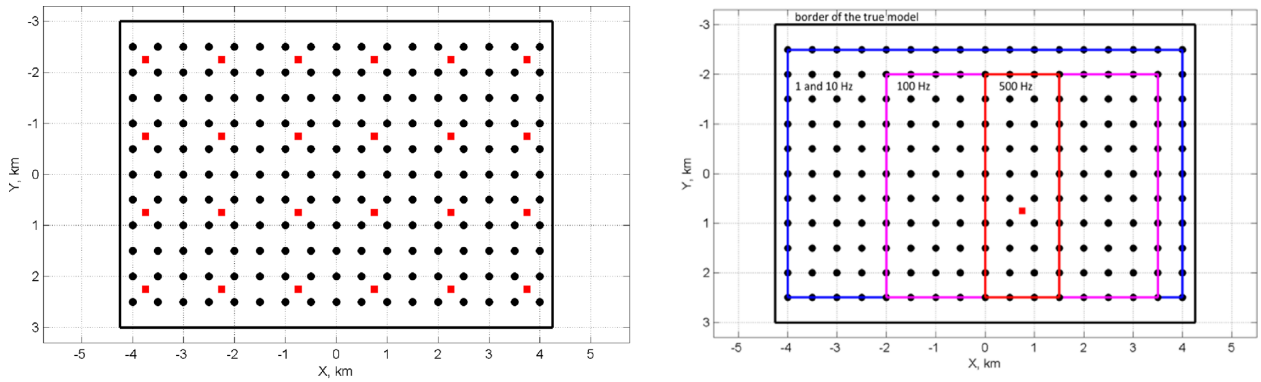

Figure 5. Panel (a): the source grid (red squares) and receiver grid (black circles) plotted over the true model (the outer black box). Panel (b): individual receiver grids (coloured boxes) for different frequencies (see numbers) for a single transmitter position (red square). Note that, frequencies 1 and 10 Hz use the same receiver grid. Also note that, the inversion model extended beyond the true model.

Table 2. Numerical grids for multi-frequency CSEM.

Frequency, Hz	Min skin-depth, m	Grid step size in core, m $h_x \times h_y \times h_z$	Max extent of grid core area, km	Max grid size	Max num of discrete variables
1	1100	200 × 200 × 50	8 × 5 × 6	69 × 53 × 152	1.7M
10	350	117 × 117 × 58	8 × 5 × 2	91 × 65 × 64	1.1M
100	110	37 × 37 × 26	5 × 4.5 × 1	171 × 143 × 69	5.1M
500	50	16 × 16 × 11	1.5 × 4.5 × 0.5	119 × 307 × 80	8.7M

limited by capabilities of available supercomputers used in our computations. There is a good reason to think that the increase in the number of frequencies inside this range would not improve the resolution significantly, though we did not specifically check this case. The frequency range is quite narrow (2.5 decades), whereas $\mathbf{E}(f)$ is usually a slowly varying function of frequency. The main difficulty in this test was the combination of highly resistive host rocks and a highly conductive target. We had to use frequencies above 10 Hz to have a noticeable inductive absorption. For example, the data (not presented here) at 0.1 Hz appeared identical to 1 Hz data, meaning that the dc limit was almost approached. At the same time a small grid step size is required to accurately approximate the electrical field in the target. For these reasons we had to limit the horizontal dimension of the FD grids at higher frequencies. Each individual monochromatic source used only a subset of receivers. Frequencies 1 and 10 Hz used the entire receiver grid; at 100 Hz

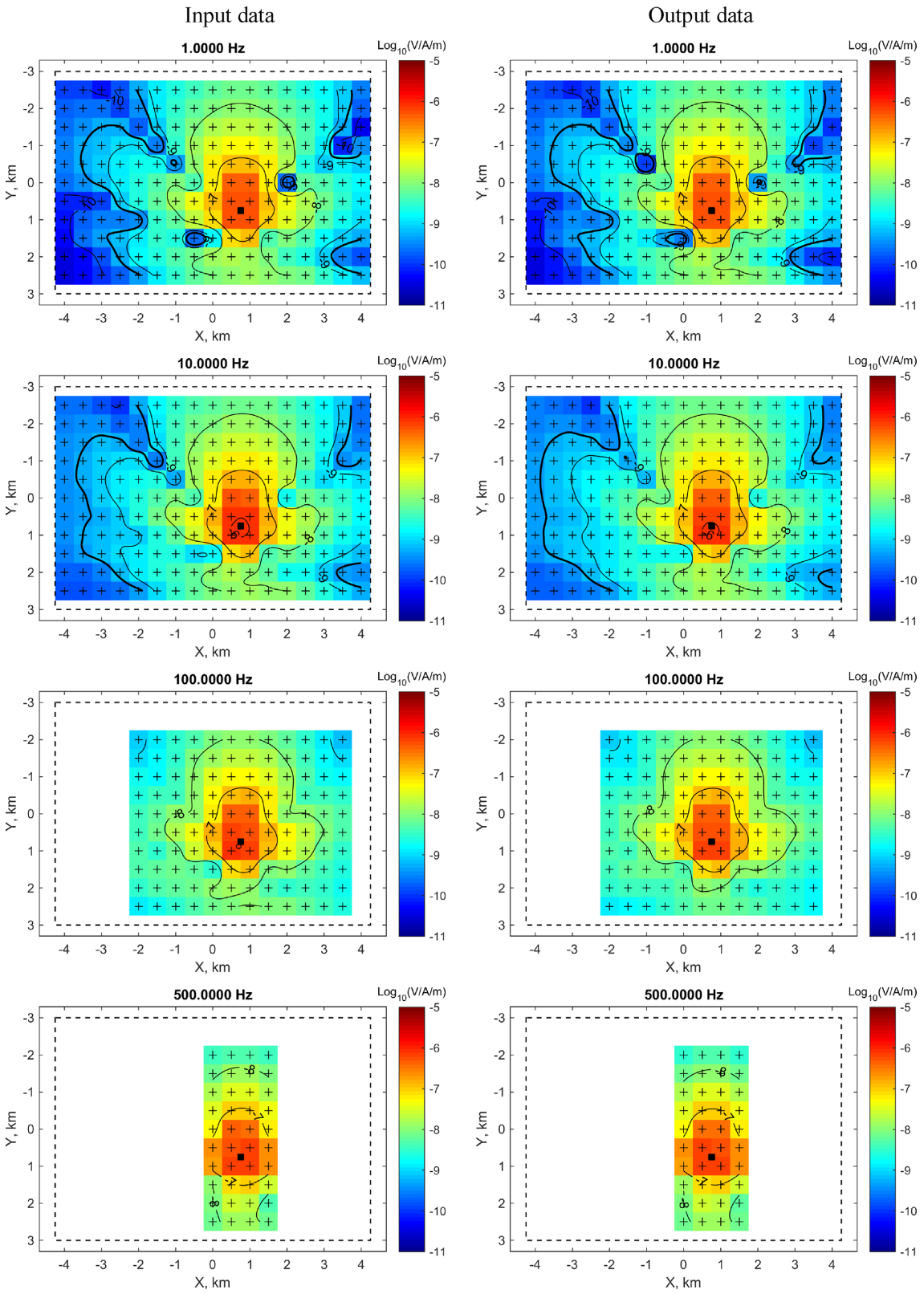

Figure 6. CSEM data in receivers for a single source at different frequencies. $\log_{10}|\mathbf{E}_y|$is shown in colour. Left column: input data. Right column: data at final iteration. The black square depicts position of the source; the + 's are the receivers. The thick black line, if present, marks the noise floor, ϵ.

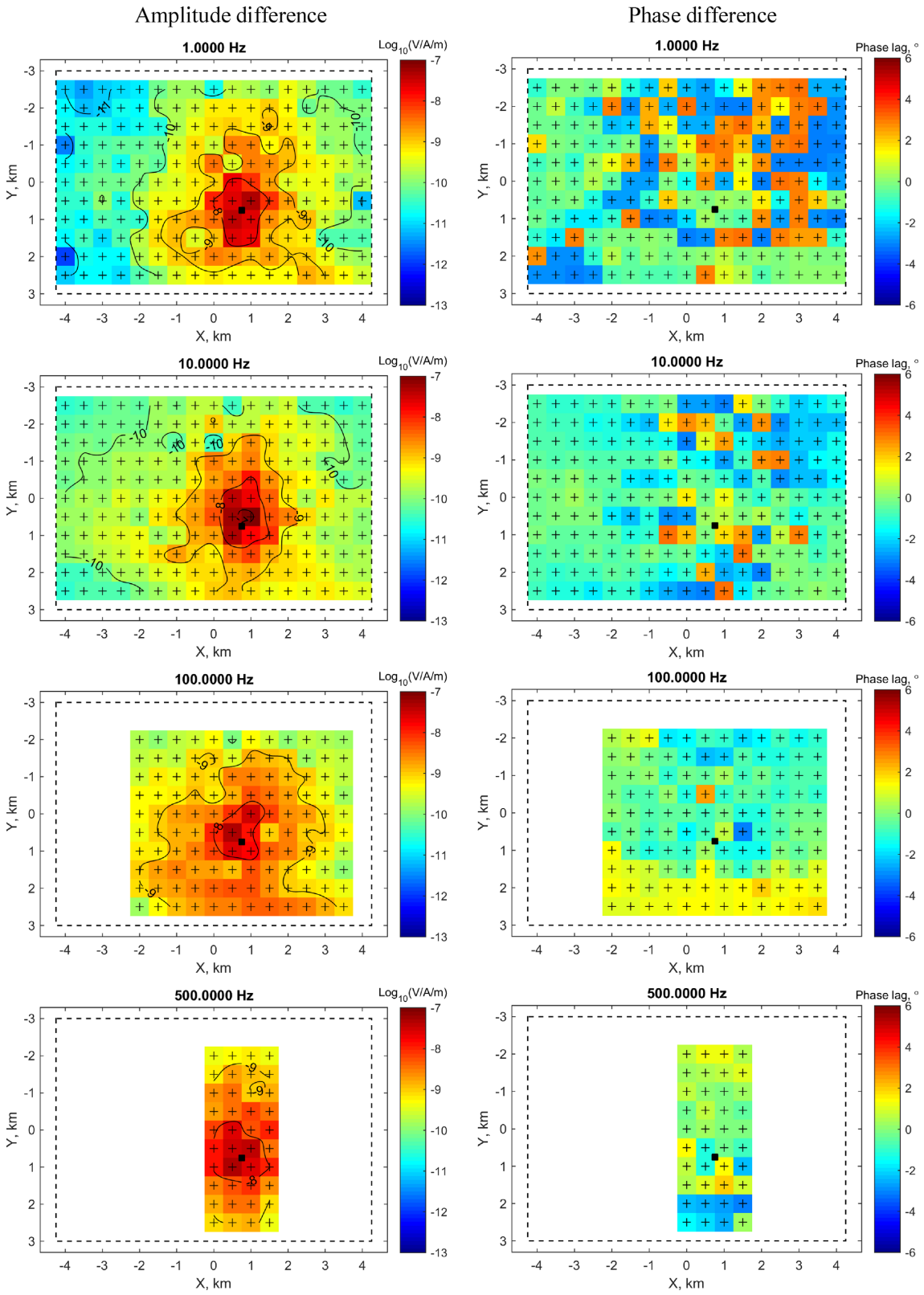

Figure 7. CSEM data residual in receivers for a single source at different frequencies. Left-hand column: amplitude difference. Right-hand column: phase difference. The black square depicts position of the source; the + 's are the receivers. The thick black line, if present, marks the noise threshold.

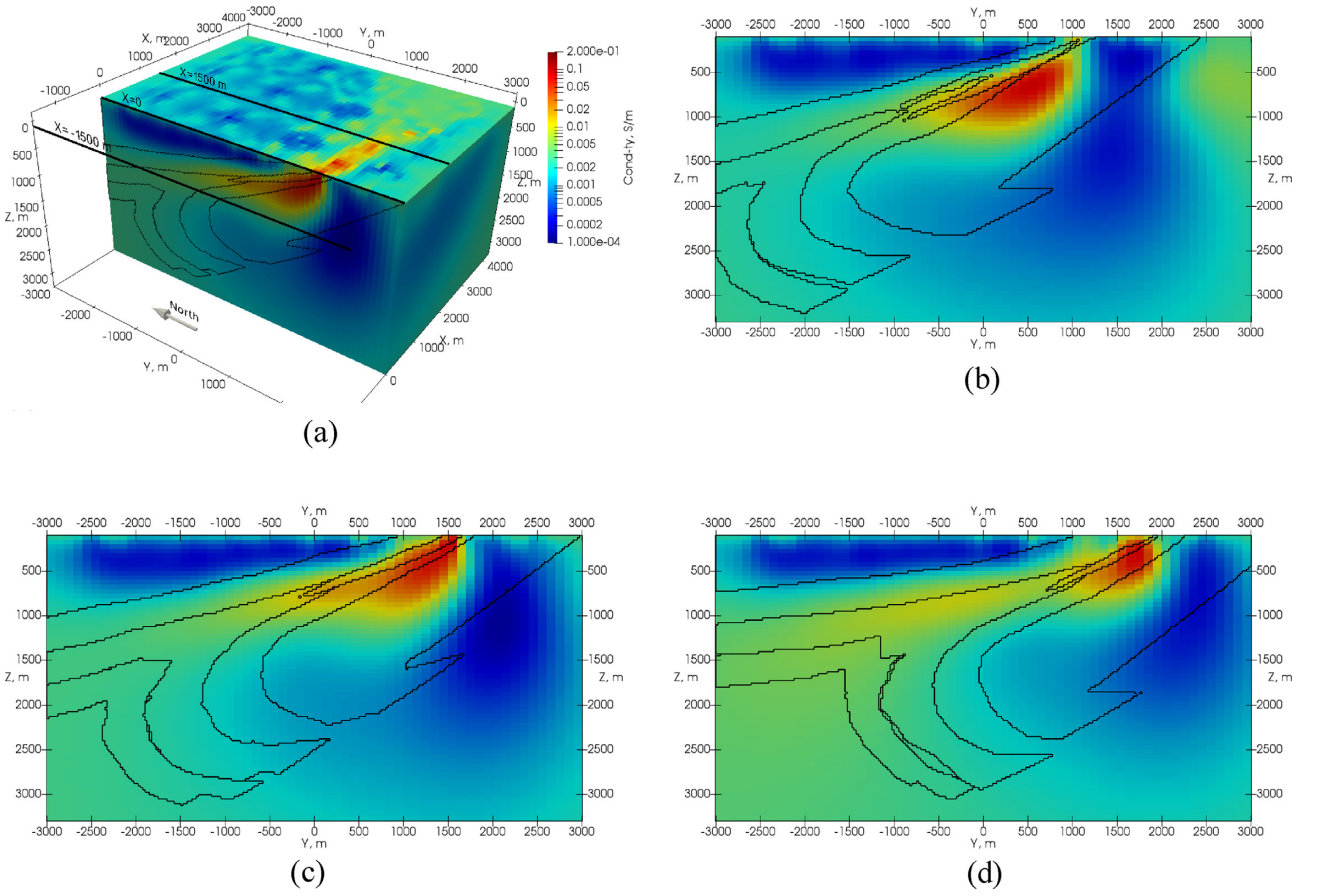

Figure 8. Panel (a): the final CSEM inversion model looking northeast cropped to the dimension of the true model; the cells with $X < 0$ were removed for visualization. Panel (b): section at $X = -1500$. Panel (c): section at $X = 0$ m. Panel (d): section at $X = 1500$ m. The black lines on top of the colour images depict the boundaries inside the true model.

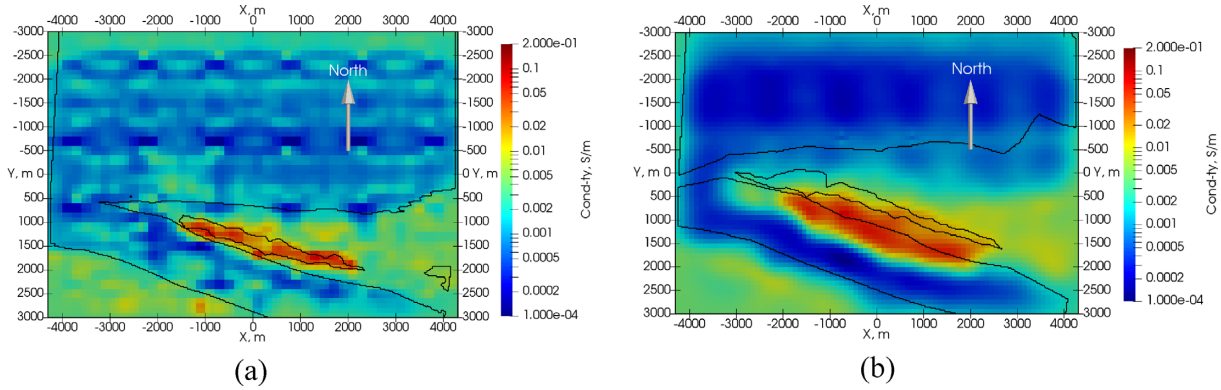

Figure 9. Plan view sections of CSEM inversion model. Panel (a): $Z = 200$ m. Panel (b): $Z = 500$ m. The black lines depict the boundaries of the orebody and high-resistive Imnyah carbonates.

the largest source-receiver separation was limited to 2750 m and 2750 m (X and Y directions, respectively); at 500 Hz the limits were set to 750 m and 2750 m, respectively. The four receiver grids for a single source are presented in Fig. 5(b). The horizontal size of a receiver grid controls the core area of the model that needs to be finely discretized. We explicitly set the vertical extent of the core numerical grids for each frequency. Parameters of numerical grids are summarized in Table 2.

We will refer all data points for a single source at a given frequency as *a shot record*. The entire data set comprises of 96 shots, 11 696 complex-valued data points it total. Synthetic data were contaminated with the circularly symmetric Gaussian noise, which implies that the real and imaginary components are both Gaussian with the same covariance and are not correlated with each other. The noise standard deviation in each i-th data point was defined as $\sigma_i = |d_i| \cdot r + \epsilon$, where d_i is a complex data point (value of the electric field), $r = 0.03$, and $\epsilon = 5 \times 10^{-10}$ V/Am (the absolute noise floor). In the following, we refer it as *the 3 per cent-noise*. We used these standard deviations both as the noise level to generate the noise and as the uncertainty floor to define entries of matrix **W**.

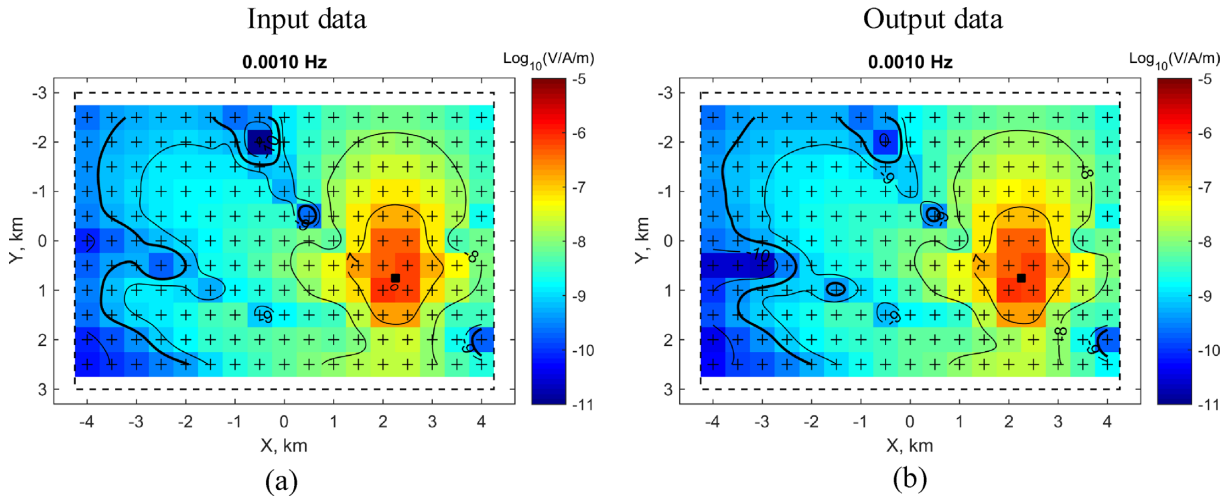

Figure 10. A representative shot of the dc data set (the electric field $\mathbf{E}_y$ in receivers). Panel (a): input data. Panel (b): the data at the final inversion iteration. The decimal logarithm of the magnitude is shown in colour. The thick black line is the noise threshold.

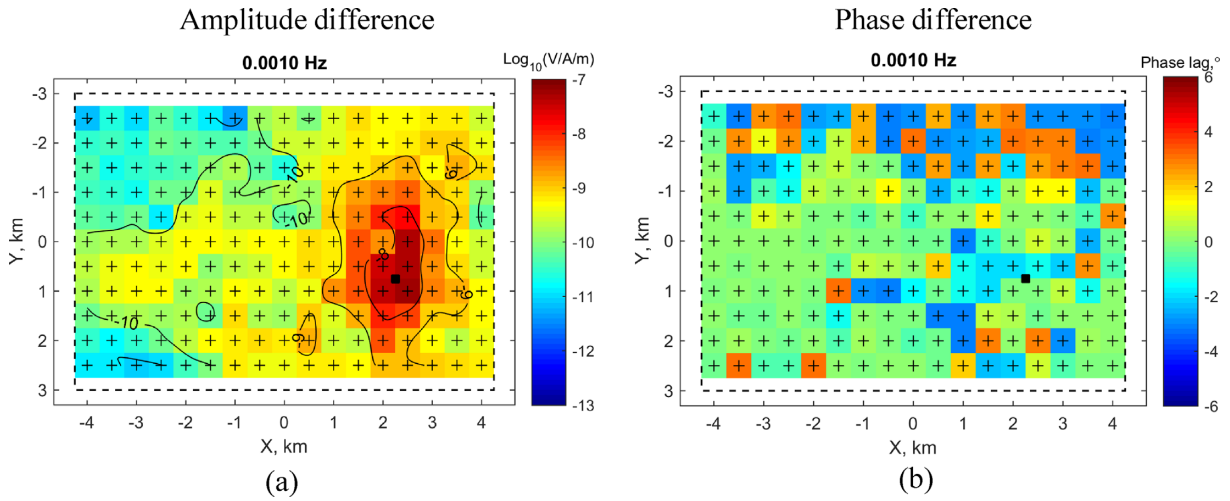

Figure 11. The dc data residual. Panel (a): amplitude difference. Panel (b): phase difference. The black square depicts position of the source; the + 's are the receivers.

Four representative shots at the same source station are shown in Fig. 6 (left column of pictures).

The inversion model consisted of 160 × 120 × 120 cells (∼2.3 M in total); each cell had dimensions of 100 m × 100 m × 50 m. The inversion model extends beyond the starting model in order to reduce the boundary effect from zero Dirichlet boundary condition imposed on the discrete Laplacian operator. We emphasize that, the number of cells in the inversion domain has limited impact on the inversion performance due to the two reasons. First, our code inverts the Hessian matrix iteratively. Thus, the number of cells in the inversion domain practically does not affect the run time nor the memory demand of the optimization part, apart from negligible contribution from the calculation of the Laplacian of the inversion model, and the input-output. Secondly, the forward-problem FD grids are independent of the inversion domain. This means that the forward modelling performance is not affected as well.

The background model consisted of the air half-space, 100 m-layer of 250 Ωm and a lower half-space of 300 Ωm. The top 100 m of the model was not changed in inversion. We would like to discuss this point in more details. We used the secondary-field approach, see Eq. (A3). If sources are placed in a domain with zero anomalous conductivity, $\sigma_a = 0$, then the computational sources, defined by $\sigma_a \mathbf{E}_b$ term, are moved away from the true sources. It increases the accuracy of FD approximation and makes dense gridding around the true sources unnecessary. This is exactly what happens in the examples presented here. The question arises what would happen if CSEM data from grounded cable sources are inverted in the presence of shallow inhomogeneities. In that case, the term $\sigma_a \mathbf{E}_b$ may become singular in the cells, where the true sources are located. Our numerical experiments (not shown here) suggest that, the amount of inhomogeneity introduced by inversion artefacts is enough to destroy the FD approximation on uniform grids. Thus, the advantages of the secondary-field approach are completely lost. Although it does not apply for the numerical examples considered nor alter the findings of this paper, we conclude that, inverting for the shallow cells requires the total-field approach, with FD grids adjusted to the sources' location, supplemented by an interpolation procedure between the inversion grid and non-uniform FD grids. We also mention that in the framework of the secondary-field approach some remedies still may be considered, see discussion in (Grayver *et al.* 2013, 2014).

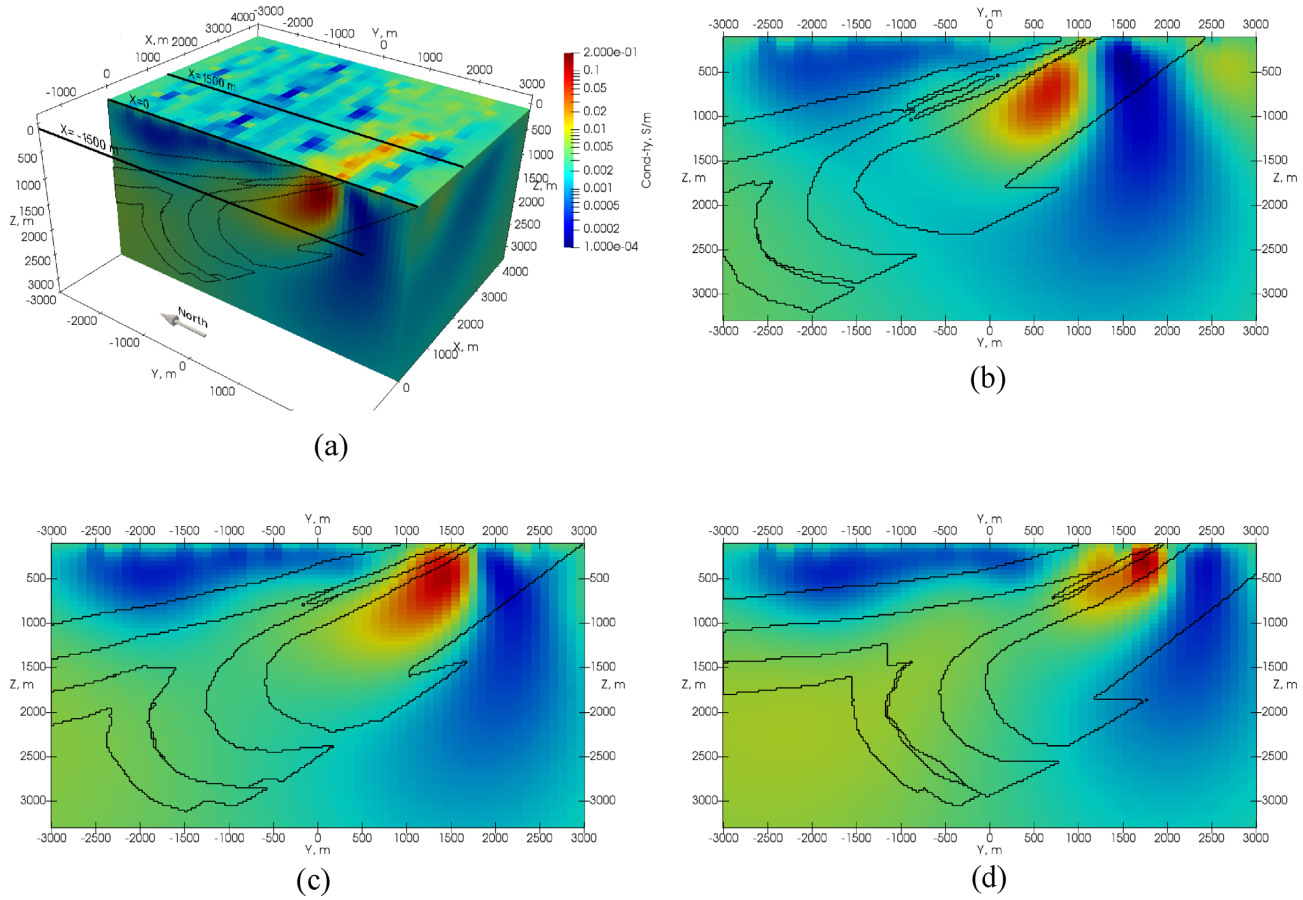

Figure 12. Panel (a): the final dc inversion model looking northeast cropped to the dimension of the true model with cells with $X < 0$ removed for visualization. Panel (b): section at $X = -1500$ m. Panel (c): section at $X = 0$ m. Panel (d): section at $X = 1500$ m. The black lines on top of the colour images depict the boundaries inside the true model.

Inversion started from the background model. The inversion was running in parallel on 42 nodes, 24 core per node, 1008 cores in total. Each node was equipped with double 12-core Intel Xeon E5-2680v3 processors running at 2.5 GHz, 128 GB RAM, and InfiniBand interconnect. In order to balance the computational load, we used the following dispatching: the 500 Hz forward problems were distributed across 24 compute nodes (1 problem per node); the 100 Hz forward problems were distributed across 12 nodes (2 problem per node); the 10 and 1 Hz forward problems were all distributed over 6 nodes in the round-robin fashion (8 problem per node). The BiCGStab tolerance in the forward problem was set to 10^{-6}. We checked that this tolerance ensured the convergence of the 3-D solution, and the match between the 3-D solution and 1-D solution for a 1-D model. The normal system of equations was solved by the CG method to 10^{-3} tolerance. We checked that the tolerance 10^{-3} provided the same model update as 10^{-4}, but differed from 10^{-2}. The CG solver was terminated prematurely on the last iteration to ensure that the final ERMS was close to 1. Inversion completed four iterations for 178 hr reducing ERMS from 10 to 1.02. The data computed with the final inversion model is presented in Fig. 6 (the right-hand column of pictures); the data residual is given in Fig. 7.

The most prominent feature of the final conductivity distribution is a strong conductive anomaly in the centre of the model, which dips to the north direction (Fig. 8a). The top cells have mosaic pattern, known as *the source footprint*, due to strong non-linearity in vicinity of transmitters and receivers. It is considered to be an inversion artefact. Three vertical sections through the final model, superimposed with boundaries in the true model, allow for a detailed comparison between the true model and the inversion outcome (Figs 8b–d).

We will focus on geological results derived from the inversion. The strong conductive anomaly is an image of the Upper Khomolho rocks. The position and shape of the anomaly is in good agreement with the true model. The resolution is somewhat worse in the vertical direction: the orebody thickness appears vertically exaggerated. Appearance of conductive shadow zones in EM methods is well established (Jones 1999; Bedrosian 2007; Kalscheuer *et al*. 2018). At the same time, the anomaly dip, the lateral extent and the position of the orebody top are determined quite satisfactory (Fig. 9).

The lower-conductive zones, which surround the central conductive anomaly, correspond to Imnyah highly resistive rocks. The bottom of the upright limb is nicely mapped. The image of the overturned limb is blurred, especially its bottom part. Nevertheless, its shape is captured to such an extent that it allows one to judge its geometry and depth. The agreement between the inversion result and the rock model is very encouraging.

4.3 Numerical experiment 2

In the second numerical experiment we compared sensitivity of the multifrequency CSEM with a dc survey provided that the source and receiver grids are equal. We do not debate the relative cost of

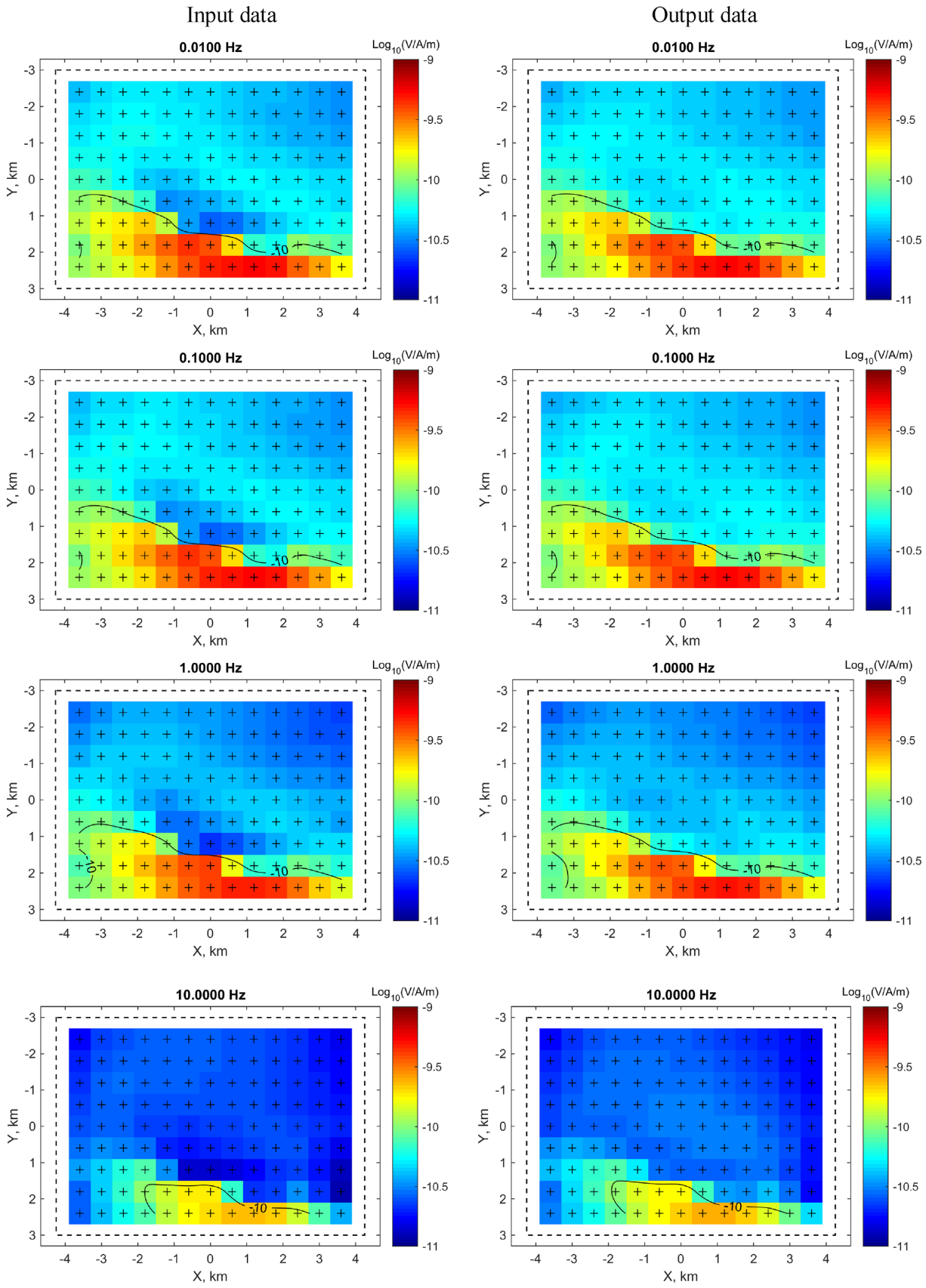

Figure 13. The single-source CSEM data. Left-hand column: synthetic electric field $\mathbf{E}_y$ at different frequencies. Right-hand column: predicted $\mathbf{E}_y$ at the end of inversion. The decimal logarithm of the magnitude is shown in colour.

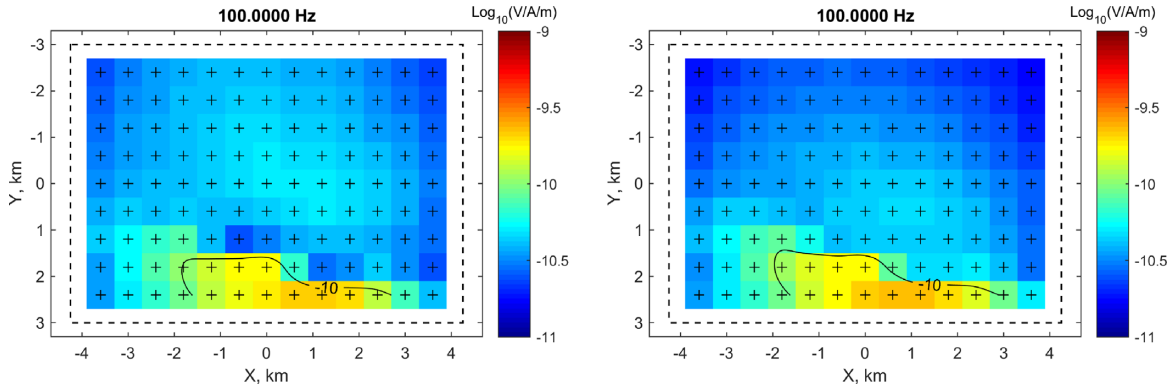

Figure 13. *Continued.*

Table 3. Numerical grids for the single-source CSEM test.

Frequency (Hz)	Min skin-depth (m)	Grid step size in core (m) $h_x \times h_y \times h_z$	Max extent of grid core area (km)	Max grid size	Max num of discrete variables
0.01	11 000	200 × 200 × 50	8 × 5 × 6	71 × 59 × 157	2M
0.1	3500	200 × 200 × 50	8 × 5 × 6	65 × 53 × 155	1.6M
1	1100	200 × 200 × 50	8 × 5 × 6	65 × 51 × 152	1.5M
10	350	117 × 117 × 58	8 × 5 × 2	83 × 63 × 64	1M
100	110	37 × 37 × 26	8 × 5 × 1	217 × 151 × 69	6.8M

the two geophysical methods, because for the land CSEM there is a limited field practice.

Using a third-party dc code program will bias the comparison, so we used the same inversion code with the source frequency as low as 0.001 Hz. The minimal skin-depth at this frequency (35 km) is much larger than maximal transmitter–receiver separation (8 km), meaning that the electric field is sampled in the near-field zone and the dc regime is achieved. We note that, a dedicated dc code may be more efficient than ours. For example, the system matrix, arising in the dc forward modelling, is real symmetric positive-definite. Consequently, in a dedicated software the system of linear equations is usually solved by the CG solver instead of BiCGStab, which roughly halves the number of required matrix–vector multiplication.

In this test we used the source and receiver grids as depicted in Fig. 5(a). We use infinitesimal dipole representation for all sources and receivers. Usually, the dc measurements are performed with long receiving and transmitting lines to increase the signal-to-noise ratio. Thus, our results will describe an optimistic scenario in terms of spatial resolution. There were 24 monochromatic sources. Each shot includes all 187 receivers. A representative synthetic shot is presented in Fig. 10(a).

In this experiment we used a FD grid with cells 200 m × 200 m × 50 m. Inversion was run on 24 nodes, which were identical to those used above. Inversion completed three iterations for 20 hr. The ERMS decreased from 8.5 to 0.99. The final data computed with the final inversion model is presented in Fig. 10(b). The data residual is given in Fig. 11. We observe that the dc inversion outcome (Fig. 12) is close to that of the multifrequency CSEM, with some minor differences. The conductive orebody appeared more smeared and its top was imaged at wrong depth. The bottom of the upper resistive body #2 was determined far less accurately. The obvious reason is the lack of resolution of dc data to shallow part of the model. The dc inversion, in contrast with the CSEM one, introduced a low-conductive anomaly in deeper northern part of the model, which is contrary to fact that that high-conductive formations #5 and #6 are there (compare Fig. 12b with Fig. 8b).

The dc inversion, as expected, demonstrated poorer resolution that the CSEM one did. However, the main orebody has been localized with satisfactory accuracy. On the other hand, the dc inversion procedure is far more economical both with regards to field work and with respect to the numerical inversion. We conclude that, in the absence of high-resistive layers above the target (which limits the depth of penetration of the dc) and in case of a strong conductivity contrast (which leads to numerical difficulties in multi-frequency multi-offset CSEM method) with overall high resistivity of the geological medium (which decreases impact of the inductive attenuation), modern dense 3-D dc measurements might be an adequate tool for surveying mining targets.

4.4 Numerical experiment 3

Geophysical operators tend to use as few sources as possible to reduce the cost of logistics. It is not uncommon to see surveys, conducted with a single source for the entire area. In this numerical experiment we simulate a single-source CSEM and study its spatial resolution.

We used the same receiver grid as before. There was a single source station, located 10 km southwards from the centre of the true model. For such a configuration the secondary-field approach is obviously advantageous, since the remote source has not to be included in the densely gridded core area. We used five frequencies: 0.01, 0.1, 1, 10 and 100 Hz. The sources and receivers were electric Y-dipoles. This configuration has much in common with CSAMT settings, especially in the fact that, a remote dipole generates the non-uniform plane wave in both cases, and we used the term CSAMT in our preliminary report (Malovichko *et al.* 2019). The biggest differences are the absence of the magnetic components (consequently, it is not a tensorial setup), the absence of another orthogonal orientation and a narrow, coarsely sampled, frequency range. The horizontal extents of the numerical grids were identical for all frequencies, but limits were imposed on the vertical dimension (Table 3).

The synthetic data are presented in Fig. 13 (left-hand column of pictures). The uncertainties in the input data were set to 3 per cent with 10^{-11} V (Am)$^{-1}$ noise floor. The initial model was the same, as before. Inversion was running on 5 nodes, 1 forward problem per node. It converged in a single iteration, reducing ERMS from 3.7 to 0.73. The run time was 5 hr. The run time was dictated by the 100 Hz forward problem. The same run time could have been obtained on only 2 nodes, grouping frequencies 0.01–10 Hz in the

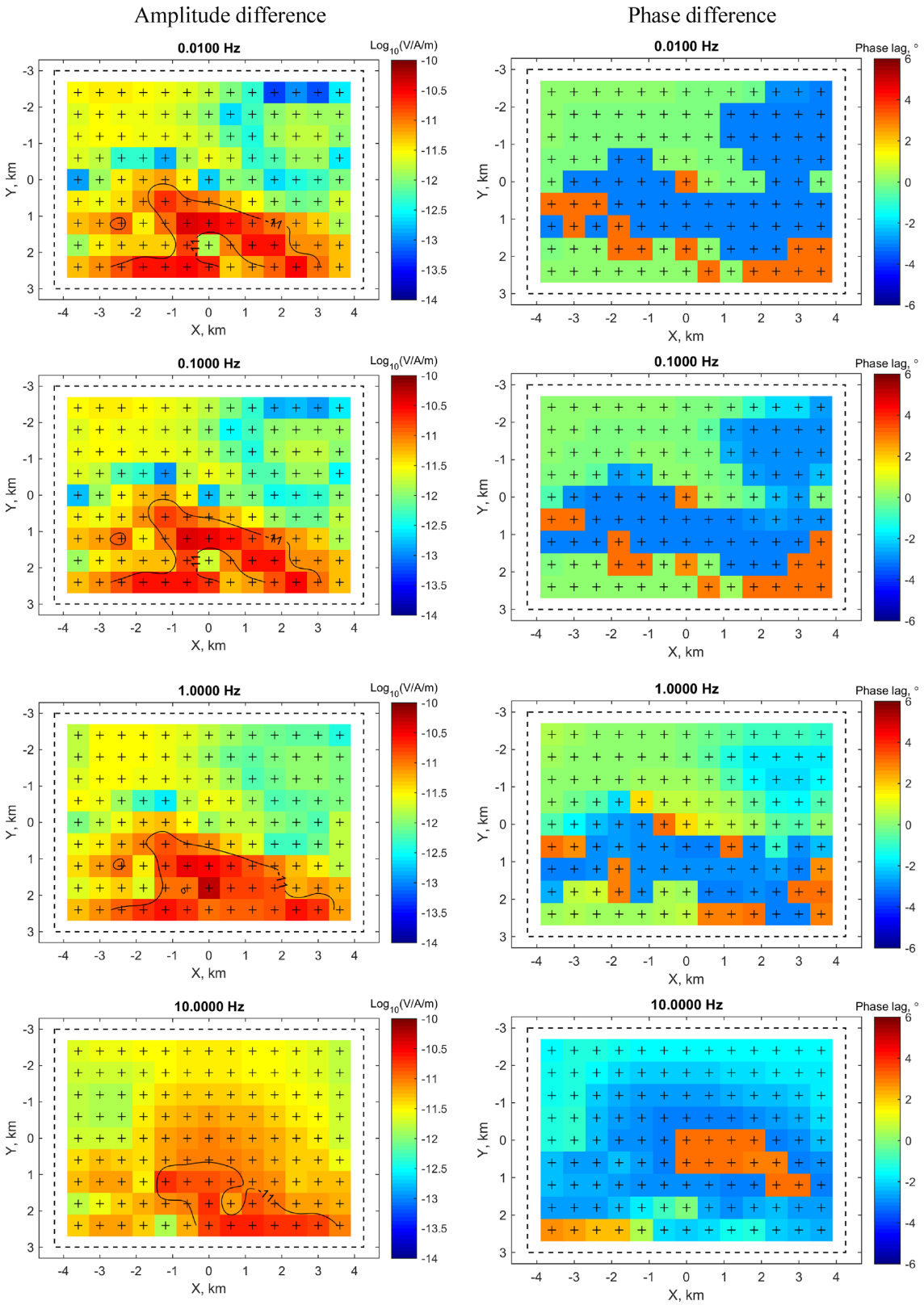

Figure 14. The single-source CSEM data residual. Left-hand columns: amplitude difference. Right-hand column: phase difference.

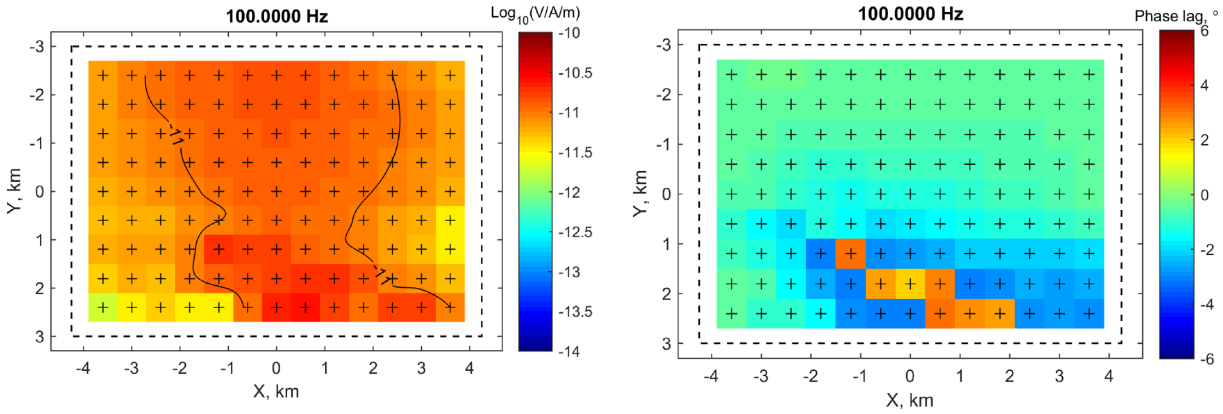

Figure 14. *Continued.*

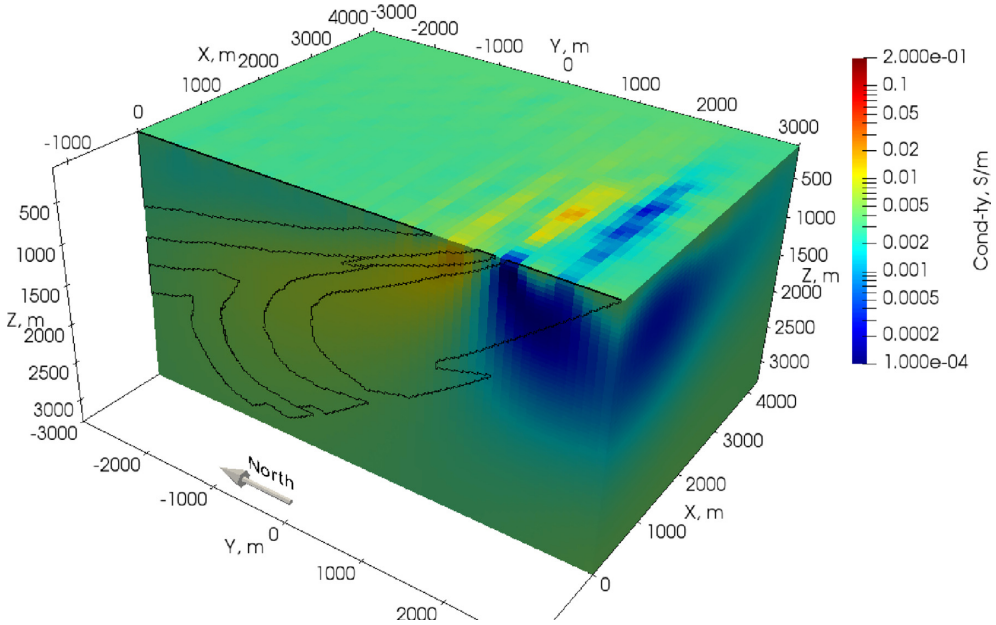

Figure 15. Section $X = 0$ through the recovered single-source CSEM conductivity model.

first node, and frequency 100 Hz on the second one. The predicted data are in good agreement with the input data (Figs 13 and 14).

The final model is presented in Fig. 15. An experienced interpreter can identify the presence of the conductive orebody and, probably, assume existence of the high-resistive body #3. However, the general quality of the single-source CSEM model is significantly inferior to the dense CSEM and dc ones.

From computational standpoint (not to mention the field measurements) the CSEM inversion with a single source is very economical. An industrial-scale 3-D inversion can be performed on just a few compute nodes (in fact, on a desktop). We believe, taking in consideration our results, that the field of mining geophysics has reached the point when such measurements should give way to more accurate exploration techniques. The question arose, however, of what is the optimal number of sources. In some studies, the use of a small number of sources, apparently, allowed to achieve an acceptable spatial resolution (Grayver *et al* 2014; Tietze *et al*. 2015; Schaller *et al*. 2018). At the same time, a rigorous estimate of the optimal number of sources requires a dedicated study. It depends on many factors: the geology of the area (the role of the inductive attenuation), frequency range, measured components of electric and/or magnetic fields, the type of transmitter, etc. Such estimates are outside the scope of this paper.

5 CONCLUSIONS

We studied the land-based multifrequency CSEM method applied to mineral exploration and compared it to the conventional dc one and to a CSEM survey with a single source. Such measurements (i) have high spatial resolution, which is always problematic in EM geophysics and (ii) the 3-D inversion of fully 3-D CSEM data is feasible with currently available codes and computing resources. Our results suggest that, using a dense 3-D CSEM data for mineral explorations can increase the quality of model reconstruction, comparing to other more frequently used methods. At the same time, in our example the improvement over conventional dc method may be not enough to justify the substantially higher cost of the CSEM survey. However, in a less resistive environment the impact of the inductive absorption can be much higher which would require the use of the CSEM method.

We believe that availability of 3-D inversion tools for a geophysical method is at least as important as logistics and equipment

considerations. After all, the cost of collecting and inverting a 3-D data set would be a fraction of a drilling program.

ACKNOWLEDGEMENTS

This research was supported by the Russian Science Foundation, project No. 18-71-10071. The authors also acknowledge the support of the University of Utah Consortium for Electromagnetic Modelling and Inversion (CEMI) and TechnoImaging. This work has been carried out using computing resources of the federal collective usage centre Complex for Simulation and Data Processing for Mega-science Facilities at NRC 'Kurchatov Institute', http://ckp.nrcki.ru/. We would like to acknowledge the Skoltech CDIES's high performance computing cluster, Zhores, for providing the computing resources that have contributed to the results reported herein. We further thank Thomas Kalscheuer and an anonymous reviewer for numerous suggestions that helped us to improve our manuscript.

REFERENCES

Bedrosian, P.A., 2007. MT+, Integrating magnetotellurics to determine Earth structure, physical state, and processes, *Surv. Geophys.,* **28**(2), 121–167.

Bretaudeau, F., Coppo, N., Wawrzyniak, P. & Penz, S., 2017. 3D land CSEM inversion with a single transmiter position, in *Proceedings of the 79th EAGE Conference and Exhibition,* EAGE.

Buryak, V.A. & Khmelevskaya, N.M., 1997. Sukhoy Log, one of the greatest gold deposits in the world: Genesis, distribution patterns, prospecting criteria (in Rissian), Dalnauka.

Chave, A. & Jones, A.(eds), 2012. *The Magnetotelluric Method: Theory and Practice,* Cambridge University Press.

Commer, M. & Newman, G.A., 2008. New advances in three-dimensional controlled-source electromagnetic inversion, *Geophys. J. Int.,* **172,** 513–535.

Constable, S., 2010. Ten years of marine CSEM for hydrocarbon exploration, *Geophysics,* **75**(5), A67–A81.

Cox, L., Wilson, G. & Zhdanov, M., 2012. 3D inversion of airborne electromagnetic data, 3D inversion of airborne electromagnetic data, *Geophysics,* **77**(4), WB59–WB69.

Cox, L.H. & Zhdanov, M.S., 2007. Large-scale 3D inversion of HEM data using a moving sensitivity domain, in *Proceedings of the 7th Annual International Meeting, Expanded Abstracts; Society of Exploration Geophysics (SEG),* pp. 467–470, Tulsa, OK, USA.

Distler, V.V., Yudovskaya, M.A., Mitrofanov, G.L., Prokof'ev, V.Y. & Lishnevskiy, E.N., 2004. Geology, composition and genesis of the Sukhoi Log noble metals deposit, Russia, *Ore Geol. Rev.,* **24,** 7–44.

Egbert, G.D. & Kelbert, A., 2012. Computational recipes for electromagnetic inverse problems, *Geophys. J. Int,* **189,** 251–267.

Farquharson, C.G. & Lelièvre, P.G., 2017. Modelling and inversion for mineral exploration geophysics: a review of recent progress, the current state-of-the-art, and future directions, in *Proceedings of Exploration 17: Sixth Decennial International Conference on Mineral Exploration,* DMEC.

Goldfarb, R.J., Baker, T., Dube, B., Groves, D.I., Hart, C.J.R. & .Gosselin, P, 2005. Distribution, character, and genesis of gold deposits in metamorphic terranes, *Econ. Geol. 100th Anniversary Volume*, pp. 407–450.

Grayver, A., Streich, R. & Ritter, O., 2014. 3D inversion and resolution analysis of land-based CSEM data from the Ketzin CO2 storage formation, *Geophysics,* **79**(2), E101–E114.

Grayver, A.V., Streich, R. & Ritter, O., 2013. Three-dimensional parallel distributed inversion of CSEM data using a direct forward solver, *Geophys. J. Int.,* **193**(3), 1432–1446.

Günther, T., Rücker, C. & Spitzer, K., 2006. Three-dimensional modelling and inversion of DC resistivity data incorporating topography - II. Inversion, *Geophys. J. Int.,* **166,** 506–517.

Jansen, J.C. & Cristall, J.A., 2017. Mineral exploration using natural EM fields, in *Proceedings of Exploration 17: Sixth Decennial International Conference on Mineral Exploration,* DMEC.

Jones, A.G., 1999. Imaging the continental upper mantle using electromagnetic methods, *Developments in Geotectonics,* Vol. **24,** Elsevier.

Kalscheuer, T., Juhojuntti, N. & Vaittinen, K., 2018. Two-dimensional magnetotelluric modelling of ore deposits: Improvements in model constraints by inclusion of borehole measurements, *Surv. Geophys.,* **39**(3), 467–507.

Kalscheuer, T. *et al.*, 2015. Joint inversions of three types of electromagnetic data explicitly constrained by seismic observations: results from the central Okavango Delta, Botswana, *Geophys. J. Int.,* **202,** 1429–1452.

Kaufman, A.A. & Keller, G.V., 1983. *Frequency and Transient Soundings,* Elsevier.

Key, K., 2016. MARE2DEM: A 2-D inversion code for controlled-source electromagnetic and magnetotelluric data, *Geophys. J. Int.,* **207**(1), 571–588.

Kim, H.J. & Kim, Y.H., 2011. A unified transformation function for lower and upper bounding constraints on model parameters in electrical and electromagnetic inversion, *J. Geophys. Eng.,* **8,** 21–26.

Large, R.R., Maslennikov, V.V., Robert, F., Danyushevsy, L.V. & Gang, Z., 2007. Multistage sedimentary and metamorphic origin of pyrite and gold in the Giant Sukhoi log deposit, Lena Gold Province, Russia, *Econ. Geol.,* **102,** 1233–1267.

Li, X. & Pedersen, L.B., 1991. Controlled source tensor magnetotellurics, *Geophysics,* **56**(9), 1456–1461.

Loke, M.H., Chambers, J.E., Rucker, D.F., Kuras, O. & Wilkinson, P.B., 2013. Recent developments in the direct-current geoelectrical imaging method, *J. appl. Geophys.,* **95,** 135–156.

Malovichko , M., Tarasov, A.V., Yavich, N. & Zhdanov, M.S., 2019, Comparing the effectiveness of CSEM, CSAMT, and DC methods on a 3D model of gold deposit. *Proceedings of the 81th EAGE Conference and Exhibition,* EAGE.

Malovichko, M., Yavich, N., Khokhlov, N. & Zhdanov, M., 2018. On the optimal strategy of three-dimensional inversion of low-frequency electromagnetic data, in *Proceedings of the 2nd Conference on Geophysics for Mineral Exploration and Mining,* EAGE.

Morten, J.P., Poudroux, J.-M. & Mittet, R., 2016. A modeling study of augmenting coarse-grid 3D controlled-source electromagnetics with data from a towed receiver array, *Geophysics,* **81**(1), E33–E42.

Newman, G.A. & Boggs, P.T., 2004. Solution accelerators for large-scale three-dimensional electromagnetic inverse problems, *IOP Inverse Problems,* **20,** S151–S170.

Newman, G.A. & Commer, M., 2005. New advances in three-dimensional transient electromagnetic inversion, *Geophys. J. Int.,* **160,** 5–32.

Oldenburg, D., Haber, E. & Shekhtman, R., 2013. Three-dimensional inversion of multisource time domain electromagnetic data, *Geophysics,* **78**(1), E47–E57.

Oldenburg, D.W. & Pratt, D.A., 2007. Geophysical inversion for mineral exploration: a decade of progress in theory and practice, in *Proceedings of Exploration 07: Fifth Decennial International Conference on Mineral Exploration,* DMEC.

Rundqist, I.K., Bobrov, V.A., Smirnova, T.N., Smirnov, M.Y., Danilova, M.Y. & Ascheulov, A.A., 1992. Etapy formirovaniya Bodaibinskogo zolotorudnogo rayona (in Russian), *Geologiya Rudnikh Mestorozdeny,* **34,** 3–15.

Schaller, A., Streich, R., Drijkoningen, G., Ritter, O. & Slob, E., 2018. A land-based controlled-source electromagnetic method for oil field exploration: an example from the Schoonebeek oil field, *Geophysics,* **83**(2), WB1–WB17.

Shore, G.A., 2017. Very large scale 3D DC resistivity mapping: inferring the location of deep structural feeders beneath surface hot-spring manifistations, in *Proceedings of Exploration 17: Sixth Decennial International Conference on Mining Exploration,* DMEC.

Strack, K.M., 1999. *Exploration with Deep Transient Electromagnetics,* pp. 374, Elsevier.

Streich, R., Becken, M., Matzander, U. & Ritter, O., 2011. Strategies for land-based controlled-source electromagnetic surveying in high-noise regions, *Leading Edge,* **30,** 1174–1181.

Stummer, P., Maurer, H. & Green, A.G., 2006. Experimental design: Electrical resistivity data sets that provide optimum subsurface information, *Geophysics,* **166,** 506–517.

Sushinskiy, L.S., 2015. *Poiskovie raboty na bolsheob'omnoe zolotoe orudenenie, localizovannoe v uglerodisto-terrigennikh kompleksakh v predelakh Eniseyskoy, Baikalo-Patomskoy i Verkhoyansko-Kolymskoy zolotorudnikh provintsiy* (in Russian), geological report, contract no. EK-04-34/09 (03.06.2013), FGUP "Central Research Institute of Geological Prospecting for Base and Precious Metals".

Tarasov, A.V. & Gurin, G.V., 2016. Prognozno-poiskovie geologo-geophysicheskiye priznaki Sukhologskogo rudnogo polya (in Russian), *Rudy i metally,* **4,** 22–47.

Tietze, K., Ritter, O. & Veeken, P., 2015. Controlled-source electromagnetic monitoring of reservoir oilsaturation using a novel borehole-to-surface configuration, *Geophys. Prospect.,* **63,** 1468–1490.

Uhlemann, S., Wilkinson, P.B., Maurer, H., Wagner, F.M., Johnson, T.C. & Chambers, J.E., 2018. Optimized survey design for electrical resistivity tomography: combined optimization of measurement configuration and electrode placement, *Geophys. J. Int.,* **214**(1), 108–121.

Vallée, M.A., Smith, R.S. & Keating, P., 2011. Metalliferous mining geophysics—state of the art after a decade in the new millennium, *Geophysics,* **76**(4), W31–W50.

Vanyan, L.L., Bobrovnikov, L.Z. & Loshenitzina, V.L., 1967. *Electromagnetic Depth Soundings,* Consultants Bureau.

Wang, F., Morten, J.P. & Spitzer, K., 2018. Anisotropic three-dimensional inversion of CSEM data using finite-element techniques on unstructured grids, *Geophys. J. Int.,* **213**(2), 1056–1072.

Wirianto, M., Mulder, W.A. & Slob, E.C., 2010. A feasibility study of land CSEM reservoir monitoring in a complex 3-D model, *Geophys. J. Int.,* **181,** 741–755.

Wood, B.L. & Popov, N.P., 2006. The giant Sukhoi Log deposit, Siberia, *Russ. Geol. Geophys.,* **47**(3), 315–341.

Yavich, N., Malovichko, M., Khokhlov, N. & Zhdanov, M., 2017. Advanced method of FD electromagnetic modeling based on contraction operator, in *Proceedings of the 79th EAGE Conference and Exhibition 2017,* EAGE.

Yavich, N. & Zhdanov, M.S., 2016. Contraction pre-conditioner in finite-difference electromagnetic modelling, *Geophys. J. Int.,* **206**(3), 1718–1729.

Yin, C.-C., Ren, X.-Y., Liu, Y.-H., Qi, Y.-F., Qiu, C.-K. & Cai, J. 2015. Review on airborne electromagnetic inverse theory and applications, *Geophysics,* **80**(4), W17–W31.

Yudovskaya, M.A., Distler, V.V., Prokofiev, V.Yu. & Akinfiev, N.N., 2016. Gold mineralisation and orogenic metamorphism in the Lena province of Siberia as assessed from Chertovo Koryto and Sukhoi Log deposits, *Geosci. Fronti.,* **7,** 453–481

Zhdanov, M.S., 2002. *Geophysical Inverse Theory and Regularization Problems,* Elsevier.

Zhdanov, M.S., 2009. *Geophysical Electromagnetic Theory and Methods,* Elsevier.

Zhdanov, M.S., 2010. Electromagnetic geophysics: notes from the past and the road ahead, *Geophysics,* **75**(5), 75A49–75A66.

Zhdanov, M.S., 2015. *Inverse Theory and Applications in Geophysics,* Elsevier.

Zhdanov, M.S., 2018. *Foundations of Geophysical Electromagnetic Theory and Methods,* Elsevier.

Zhdanov, M.S., Alfouzan, F., Cox, L., Alotaibi, A., Alyousif, M., Sunwall, D. & Endo, M., 2018. Large-scale 3D modeling and inversion of multiphysics airborne geophysical data: a case study from the Arabian Shield, Saudi Arabia, *Minerals,* **8**(7), 271.

Zhdanov, M.S. & Keller, G., 1994. *The Geoelectrical Methods in Geophysical Exploration,* Elsevier.

Čuma, M., Cox, L. & Zhdanov, M.S., 2016. Paradigm change in interpretation of AEM data by using a large-scale parallel 3D inversion, in *Proceedings of the Near Surface Geoscience 2016-First Conference on Geophysics for Mineral Exploration and Mining,* EAGE.

Čuma, M., Gribenko, A. & Zhdanov, M.S., 2017. Inversion of magnetotelluric data using integral equation approach with variable sensitivity domain: application to Earthscope MT data, *Phys. Earth planet. Inter.,* **270,** 113–127.

SUPPORTING INFORMATION

Supplementary data are available at *GJI* online.

sukhoi_log.tar.gz

Please note: Oxford University Press is not responsible for the content or functionality of any supporting materials supplied by the authors. Any queries (other than missing material) should be directed to the corresponding author for the paper.

APPENDIX A. JACOBIAN MATRIX-VECTOR PRODUCTS

In this section, we provide details about computation of the products involved in (7) and (8). For brevity, we will omit the index of kth MPI rank and omit the internal summation, required if there are more than one source dispatched to this rank. Thus, we consider the following expressions:

$$\mathbf{y} = \mathbf{J}\mathbf{x}, \mathbf{x} \in R^M, \boldsymbol{y} \in C^N, \tag{A1}$$

and

$$\mathbf{w} = \mathbf{J}^*\mathbf{v}, \mathbf{w} \in R^M, \mathbf{v} \in C^N, \tag{A2}$$

where M is the number of cells in the inversion model (the same for every source), and N is the number of receivers for a selected source.

First, we reformulate problem (1) using the anomalous-field approach (Zhdanov 2002):

$$curl\ curl\ \mathbf{E}_\mathrm{a} - i\omega\mu_0\sigma\mathbf{E}_\mathrm{a} = i\omega\mu_0\sigma_a\mathbf{E}_\mathrm{b}, \tag{A3}$$

where $\mathbf{E}_\mathrm{a}$ and $\mathbf{E}_\mathrm{b}$ are the anomalous and background parts of electric field, respectively: $\mathbf{E} = \mathbf{E}_\mathrm{a} + \mathbf{E}_\mathrm{b}$, and σ_a and σ_b are the anomalous and background parts of the conductivity: $\sigma = \sigma_a + \sigma_b$. Discretizing (A3) with a non-uniform grid, we introduce quantities $\mathbf{e}_\mathrm{b}$, $\mathbf{e}_\mathrm{a}$, $\mathbf{e}$, which are the discrete analogs of $\mathbf{E}_\mathrm{b}$, $\mathbf{E}_\mathrm{a}$, and $\mathbf{E}$, respectively. We also introduce diagonal matrices $\boldsymbol{\Sigma}_\mathrm{b}$ and $\boldsymbol{\Sigma}$, which are correspond to σ_b, and σ, respectively, and define matrix $\boldsymbol{\Sigma}_\mathrm{a} = \boldsymbol{\Sigma} - \boldsymbol{\Sigma}_\mathrm{b}$. The FD forward problem (A3) corresponds to the following system of linear equations:

$$\mathbf{A}\mathbf{e}_\mathrm{a} = i\omega\mu_0\boldsymbol{\Sigma}_\mathrm{a}\mathbf{e}_\mathrm{b}, \tag{A4}$$

where $\mathbf{A} \in C^{n\times n}$ is a system matrix, with n the number of internal edges in the FD grid. The system matrix in (A4) has the form $\mathbf{A} = \mathbf{R} - i\omega\mu_0\boldsymbol{\Sigma}$, where $\mathbf{R}$ is a matrix of the FD $curl\ curl$ operator.

Eq. (A4) defines a FD forward modelling operator A_{FD} that maps from σ_a to $\mathbf{e}_\mathrm{a}$ and implies solving linear problem (A4). By definition, $\delta A_{FD}(\sigma_\mathrm{a}) = \mathbf{F}\,\delta\sigma_\mathrm{a}$, where is $\mathbf{F}$ the Fréchet derivative of A_{FD}. Since $\mathbf{e}_\mathrm{a} = A_{FD}\,(\sigma_\mathrm{a})$, it follows that, to compute product $\mathbf{F}\,\delta\sigma_\mathrm{a}$ we must compute the variation $\delta\boldsymbol{e}_a$ with respect to $\delta\sigma_\mathrm{a}$. For the following it is convenient to work the equivalent form of (A4):

$$\mathbf{A}\mathbf{e}_\mathrm{a} = i\omega\mu_0\boldsymbol{\Xi}_\mathrm{b}\sigma_\mathrm{a}, \tag{A5}$$

where a diagonal matrix $\boldsymbol{\Xi}_\mathrm{b} = diag(\mathbf{e}_\mathrm{b})$, $\boldsymbol{\sigma}_a$ is the diagonal of $\boldsymbol{\Sigma}_\mathrm{a}$. Taking the first variation of (A5), we have

$$\mathbf{A}\,\delta\mathbf{e}_\mathrm{a} = i\omega\mu_0\boldsymbol{\Xi}\,\delta\sigma_\mathrm{a} \tag{A6}$$

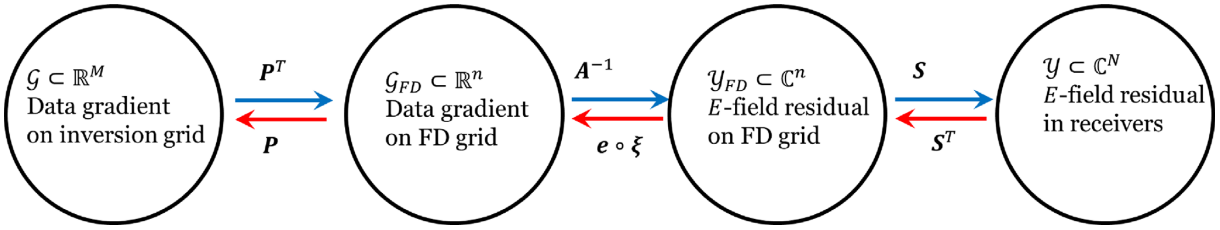

Figure A1. Interplay between several functional spaces involved in computation of act of the Fréchet operator and its conjugate. The blue arrows (left to right) indicate the sequence required to compute the product $\mathbf{Jx}$. The red arrows (right to left) indicate the sequence required to compute product $\mathbf{J}^*\mathbf{v}$. Operator $\mathbf{e} \circ \boldsymbol{\xi}$ is explained below Eq. (A13).

where a diagonal matrix $\boldsymbol{\Xi} = diag(\mathbf{e})$ (i.e. the total-field solution for the unperturbed problem). We conclude that, to compute product $\mathbf{a} = \mathbf{Fb}$ for two arbitrary vectors $\mathbf{a} \in C^n$ and $\mathbf{b} \in R^n$, we must solve the following linear system:

$$\mathbf{a} = \mathbf{A}^{-1}\, i\omega\mu_0 \boldsymbol{\Xi}\mathbf{b} \tag{A7}$$

Now, we introduce two interpolation operators. Interpolation operator $\mathbf{S} \in R^{N\times n}$ relates the data to the edge-based discrete solution:

$$\mathbf{d} = \mathbf{Se}. \tag{A8}$$

Interpolation operator $\mathbf{P} \in R^{M\times n}$ describes relationship between conductivities defined on edges of the FD grid, and conductivities sampled at centres of the inversion model grid. Additionally, entries of the model vector are related to the conductivities by a non-linear transform $f(\sigma)$. For example, $f(\sigma) = \log_{10}\sigma$. We used the unified transform of Kim & Kim (2011). It follows:

$$\mathbf{m} = f(\mathbf{P}\boldsymbol{\sigma}), \tag{A9}$$

where $\boldsymbol{\sigma}$ is a vector of conductivities at FD edges. In calculations relative to the Fréchet derivatives we used the trilinear interpolation. Thus, we have the following relation:

$$\frac{\partial \mathcal{A}}{\partial m} = \frac{\partial \mathcal{A}}{\partial \sigma}\mathbf{P}^{\mathrm{T}}\mathbf{D}, \tag{A10}$$

where $\mathbf{D}$ is a diagonal matrix with $(\frac{df}{d\sigma})^{-1}$ on its diagonal. For example, if $f(\sigma) = \log_{10}\sigma$, then $D_{ii} = diag(\sigma_i \ln 10)$. Combining everything together, we have

$$\mathbf{y} = \mathbf{Jx} = \mathbf{S}\,\mathbf{A}^{-1} i\omega\mu_0 \boldsymbol{\Xi}\mathbf{P}^{\mathrm{T}}\mathbf{Dx}. \tag{A11}$$

So, product (A1) is computed by the following sequence (see also Fig. A1, the blue path):

(1) take a vector $\mathbf{x} \in R^M$,
(2) apply $\mathbf{D}$,
(3) interpolate from inversion grid to FD grid by applying $\mathbf{P}^{\mathrm{T}}$,
(4) compute point-wise product with a solution of the compute point-wise product with a solution of theunperturbed $\mathbf{e}$,
(5) solve a system of linear equations with matrix $\mathbf{A}$,
(6) interpolate the solution from the FD grid to receivers.

Taking conjugate of (A7) one can find expression for $\mathbf{F}^*$. We have:

$$\mathbf{b} = \mathbf{F}^*\mathbf{a} = -\boldsymbol{\Xi}^*(\mathbf{A}^*)^{-1} i\omega\mu_0\mathbf{a}. \tag{A12}$$

In the right-hand side of (A12) we have a point-wise product of conjugated solution of the unperturbed problem with the solution of the conjugated problem:

$$\boldsymbol{\Xi}^*\,(\mathbf{A}^*)^{-1} i\omega\mu_0\mathbf{a} = \mathbf{e} \circ \boldsymbol{\xi}, \tag{A13}$$

where $\circ$ means the point-wise multiplication, $\boldsymbol{\xi}$ is a solution to the conjugated problem:

$$\mathbf{A}^*\boldsymbol{\xi} = -i\omega\mu_0\,\mathbf{a}. \tag{A14}$$

Finally, we have:

$$\mathbf{w} = \mathbf{J}^*\mathbf{v} = -\mathbf{D}^{\mathrm{T}}\mathbf{P}\boldsymbol{\Xi}^*(\mathbf{A}^*)^{-1} i\omega\mu_0\mathbf{S}^{\mathrm{T}}\mathbf{v}. \tag{A15}$$

In summary, the sequence of steps needed to compute product (A2) is as follows (see also the red path in Fig. A1):

(1) take a vector $\mathbf{v} \in C^N$ and apply $\mathbf{S}^{\mathrm{T}}$,
(2) solve a conjugate linear problem for $\boldsymbol{\xi}$,
(3) compute a point-wise product of $\boldsymbol{\xi}$ with conjugated solution of unperturbed problem, $\mathbf{e}$,
(4) interpolate from FD grid to inversion grid by applying $\mathbf{P}$,
(5) scale the vector by applying $\mathbf{D}$.